

CHANDRA OBSERVATIONS OF THE X-RAY JET IN CENTAURUS A

R. P. KRAFT, W. R. FORMAN, C. JONES, AND S. S. MURRAY
Harvard-Smithsonian Center for Astrophysics, 60 Garden Street, MS-31, Cambridge, MA 02138

AND

M. J. HARDCASTLE AND D. M. WORRALL
University of Bristol, Department of Physics, Tyndall Avenue, Bristol BS8 1TL, UK

Received 2001 July 26; accepted 2001 December 7

ABSTRACT

We present high angular resolution X-ray images and spectra from two *Chandra* AXAF CCD Imaging Spectrometer (ACIS-I) observations of the X-ray jet in the nearby radio galaxy Cen A. We find that the X-ray emission from the jet is composed of a low surface brightness diffuse component extending continuously from within at least 60 pc of the active nucleus into the northeast radio lobe 4 kpc from the nucleus, along with 31 discrete compact knots, most of which are extended at the resolution of our observation. We find that there are small but significant differences between the X-ray and radio morphologies of the inner jet at the arcsecond level, making it unlikely that a single, spatially coincident population of ultrarelativistic electrons is responsible for the emission in both energy regimes. We suggest that the X-ray knots of the inner jet are indeed the sites of particle acceleration and shocks and that the X-ray and radio knot offsets are caused by a combination of particle diffusion and energy loss. These offsets may be a common feature of all jets in radio galaxies, or at least jets in FR I galaxies, and may be fundamental to the physics of such jets. They are best observed in Cen A because the source is so close. Even though the X-ray and radio knots are offset in position and there are variations of more than a factor of 3 in the ratio of X-ray to radio flux density in the inner jet, the radio to X-ray two-point spectral indices at the X-ray knots are not unusually flat and are consistent with those observed in other X-ray jets seen in FR I galaxies such as M87 and 3C 66B. We find the width of the jet in the X-ray bandpass to be narrower than that measured in the radio along most of its length. The X-ray spectra of several regions of the jet are well fitted by absorbed power-law models with photon indices ~ 2.2 – 2.5 , although the spectrum of one bright knot located ~ 1 kpc from the nucleus (knot B) is harder (photon index = 2.0).

Subject headings: galaxies: active — galaxies: individual (Centaurus A, NGC 5128) — galaxies: jets — X-rays: galaxies

1. INTRODUCTION

Centaurus A (NGC 5128) is the nearest ($d = 3.4$ Mpc) active galaxy to the Milky Way and has been well studied across the entire electromagnetic spectrum (Israel 1998). Its proximity allows the features of an active galaxy to be studied at the highest linear spatial resolution ($1'' \sim 17$ pc at the distance of Cen A). Optically, Cen A appears to be an elliptical galaxy crossed by a dark dust lane through the center, which is thought to be the result of a merger with a small spiral galaxy (Schiminovich et al. 1994). Previous radio observations of Centaurus A have detected a bright radio core, a superluminal nuclear jet (Tingay et al. 1998), a one-sided kiloparsec-scale jet extending $6'$ northeast of the nucleus (Burns, Feigelson, & Schreier 1983), two radio lobes northeast and southwest of the nucleus, and extended low surface brightness diffuse emission spanning several degrees on the sky. It is often considered to be the prototypical Fanaroff-Riley (FR) class I low-luminosity radio galaxy.

Prior to the launch of *Chandra*, X-ray emission had been detected from the knots in the jets, or hotspots in the lobes, of seven radio galaxies (Harris 2002), but we are far from a detailed understanding of the mechanisms responsible for this emission. This has partly been the result of the limited angular resolution of X-ray observatories preventing a detailed comparison of jet features across a wide sample of galaxies. This has changed with the launch of the *Chandra X-Ray Observatory*. Recent *Chandra* observations of FR I

radio galaxies have shown that jet X-ray emission may be a common feature of all such galaxies (Worrall, Birkinshaw, & Hardcastle 2001; Hardcastle, Birkinshaw, & Worrall 2001), implying that the production of X-ray emission may be fundamental to the nature of such jets.

Cen A is one of two FR I galaxies in which an X-ray jet had been detected prior to *Chandra* (M87 being the other; Biretta, Stern, & Harris 1991) and, as the closest such galaxy, provides an opportunity to study jet physics at the highest linear resolution. Previous X-ray observations of Cen A have detected X-ray emission along much of the length of the jet and bright enhancements at the locations of the radio knots of the inner jet (Schreier et al. 1979; Feigelson et al. 1981; Döbereiner et al. 1996; Turner et al. 1997). Based largely on the similarities of the X-ray and radio morphologies, it has been argued that a single population of ultrarelativistic electrons is responsible for the emission in both the radio and X-ray regimes (Feigelson et al. 1981). Recent *Chandra* High Resolution Camera (HRC) observations of Cen A suggested small but significant differences in the spatial morphology of the jet in the X-ray and radio bandpasses (Kraft et al. 2000).

No optical or infrared emission from the jet at the positions of the bright X-ray knots of the inner jet has been seen. The upper limits placed by the *Hubble Space Telescope* Wide Field and Planetary Camera 2 (*HST*/WFPC2) and NICMOS observations, however, are well above an extrapolation of the radio to X-ray flux (Marconi et al. 2000). The

inner 1 kpc of the jet passes through the dust lane of the galaxy, making detection of any optical component difficult. Several optical filaments have been detected in the vicinity of the jet and northeast radio lobe, but their relationship to the X-ray/radio jet, if any, is unclear (Brodie & Bowyer 1985; Morganti et al. 1991, 1992; Israel 1998). Infrared (1.25 μm) emission extending $\sim 10''$ from the nucleus along the position angle of the jet has been detected, but it was argued that while this emission is probably related to the jet, it is not the result of synchrotron radiation from relativistic particles (Joy et al. 1991).

In this paper, we present preliminary results from the analysis of two ~ 36 ks *Chandra* ACIS-I observations of the jet in Cen A. The unprecedented angular resolution and sensitivity of *Chandra* have allowed us to resolve many features of the jet not previously seen. We present spectra of the brightest knots and diffuse emission in the jet and make a detailed comparison of the jet's X-ray and radio morphology. The goal of this paper is to present images, spectra, and preliminary results from these observations. A more detailed interpretation and discussion of these results will be presented in a future publication. Analysis of other aspects of these observations, including the X-ray point source population, emission from the hot interstellar medium, and emission from the radio lobes will be presented also in separate publications (Kraft et al. 2001). We assume a distance of 3.4 Mpc to Cen A throughout this paper.

2. INSTRUMENTATION AND OBSERVATIONS

The *Chandra* telescope has an imaging resolution of better than $1''$ on-axis. The 50% encircled energy diameter has been measured to be $\sim 0''.6$ (*Chandra* Proposers Guide 2001), and sources separated by $\leq 0''.5$ on-axis have been resolved (Chartas et al. 2000). The imaging degrades significantly for sources more than $1'$ off-axis. At $3'$ from the center of the field of view, 90% of the encircled energy is contained within a diameter of $3''$. The sensitivity of the ACIS-I instrument extends from 0.4 to 10 keV. A more detailed discussion of the capabilities of the *Chandra*/ACIS-I instrument is contained elsewhere (Weisskopf et al. 2000; *Chandra* Proposers Guide 2001). The pointing and focal plane position for each observation were chosen so that the central region of the galaxy, including the nucleus, the jet, the southwest radio lobe, and most of the point sources and diffuse emission from the hot interstellar medium (ISM) were located within one CCD (the I3 chip).

The raw events were filtered to include only *ASCA* grades 0, 2, 3, 4, and 6. All events below 0.4 keV and above 5 keV were removed. The response of the ACIS-I drops rapidly below 0.4 keV, so that most of the events below this are either background or higher energy events in the tail of the energy redistribution function. Above 5 keV, most of the events are either particle background events or events in the point-spread function (PSF) wings from the bright nucleus. All events at node boundaries were removed because of uncertainties in grade reconstruction. All events with pulse height invariant channel (PI) equal to 0, 1, or 1024 were removed as they represent unphysical signals; hot CCD columns and pixels were removed using the standard table provided by the *Chandra* X-Ray Center (CXC). Short-term transients due to cosmic rays that produced events in three or more consecutive frames that could mimic a point

source (L. P. van Speybroeck 2000, private communication) were removed as well.

Cen A was observed twice, on 1999 December 5 and 2000 May 17, with the ACIS-I instrument. The exposure times for the two observations (OBSIDs 00316 and 00962) were 35,856 and 36,510 s. The data were examined for periods of high background or problems with the aspect solution, but none were found. The aspect solution for *Chandra* observations is generally good to $2''$ or better (Aldcroft et al. 2000), but we have independently verified the aspect solution of both data sets by comparing the positions of X-ray point sources at the edge of the field of view with stellar positions tabulated in the USNO A2.0 catalog (Monet 1998) and estimate that our absolute astrometry is accurate to within $\sim 0''.5$ (Kraft et al. 2001). The field of view (FOV) for each of the observations and the position of best focus are shown in Figure 1 superposed on an optical Digitized Sky Survey (DSS) image.

The raw, co-added X-ray image in the 0.4–5 keV band-pass binned at $2'' \text{ pixel}^{-1}$ is shown in Figure 2. The nucleus is clearly visible, along with the X-ray jet extending to the northeast, many point sources, emission from the hot ISM, and emission coincident with the southwest radio lobe. This image has not been exposure corrected. The radial stripes pointing from the nucleus are the result of removing the frame transfer streak caused by out-of-time events. The other linear features around the image are gaps between the various CCDs in one or the other of the exposures. An adaptively smoothed, co-added, exposure-corrected X-ray image of Cen A in the 1–3 keV band is shown in Figure 3.

We also use radio observations of Cen A made at 8.4 GHz between 1990 October and 1991 November with the NRAO Very Large Array (VLA),¹ consisting of approximately 2 hr on-source integration time in each of the A, B, C, and DnC arrays. The data were reduced in the standard manner using AIPS and then combined (after correcting for variations in the flux density of the core) to produce a single u - v data set, sensitive to structure with a largest scale of $\sim 100''$ and with a maximal resolution of $0''.9 \times 0''.2$. The radio maps presented in this paper are all made from this full data set with appropriate tapering and weighting of the u - v plane. The nominal dynamic range of the maps (peak to off-source rms noise) is about 10^4 , but their fidelity is limited by residual phase and amplitude artifacts about the 7 Jy core. We compared the position of the radio core in this data set with its position in archival Australia Telescope Compact Array (ATCA) observations at a similar frequency and found that there was a small ($\sim 2''$) offset between the two data sets. We attribute this difference to the use of a distant ($\sim 30^\circ$) phase calibrator in the VLA observations together with the heavy use of self-calibration in the data reduction; the ATCA observations, which use a nearby phase calibrator and were only lightly self-calibrated, are likely to have better positional accuracy. We have therefore shifted the VLA data so that the core position agrees with that determined from the ATCA data. After this adjustment, we find that the X-ray and radio positions of the nuclei and the first bright X-ray/radio knot AX1/A1 agree to within the absolute aspect uncertainty of $\sim 0''.5$ of the X-ray data.

¹ The National Radio Astronomy Observatory is a facility of the National Science Foundation operated under cooperative agreement by Associated Universities, Inc.

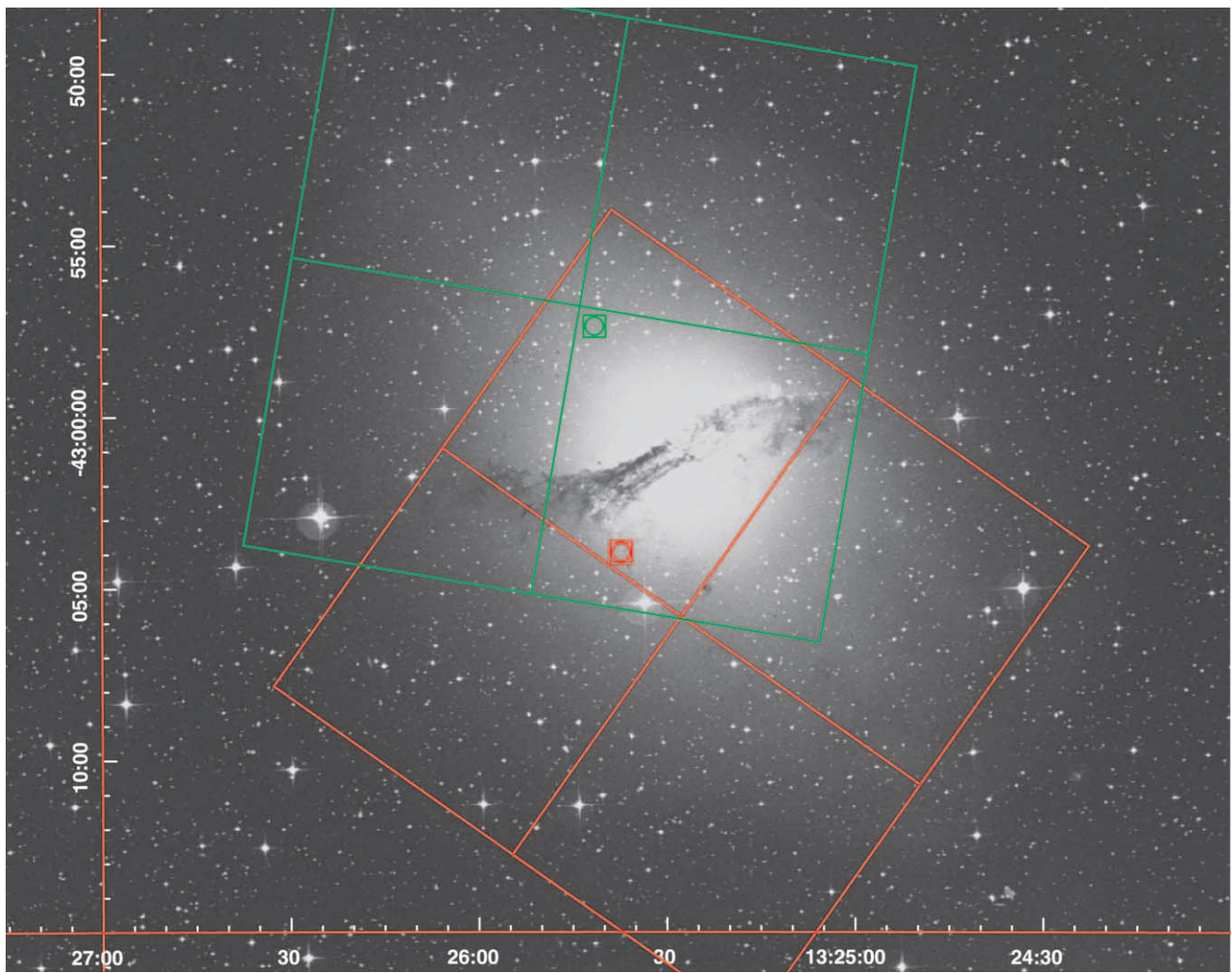


FIG. 1.—FOV of the two *Chandra* observations (OBSID 00316: white; OBSID 00962: red) overlaid onto an optical DSS image (*J* band) of Cen A. Both observations were aligned so that the central region of Cen A, including all of the X-ray jet, was well centered on the ACIS I3 CCD. Coordinates are J2000.0.

3. RESULTS

3.1. *X-Ray Morphology of the Jet*

An adaptively smoothed, co-added, exposure-corrected image of the Cen A jet in the 0.4–2.5 keV bandpass is shown in Figure 4. The nucleus is located in the southwest corner of the image, and the jet extends to the northeast. The count rate from the active nucleus in the *Chandra* bandpass is large (~ 6 counts s^{-1}) and the unusual shape of the nucleus in this image is an artifact of pileup in the ACIS-I detector. Pileup occurs when more than one event is incident on the detector in the same or adjacent pixels in less than the frame time. For moderate count rates (0.01–0.1 counts s^{-1}), this distorts the observed pulse height spectrum, since there is no way to determine if a pixel contains multiple events. At high count rates, such as that for the Cen A nucleus, the event morphologies tend to migrate to grades that are not telemetered to the ground and are lost. The figure shows that diffuse emission from the jet is observed continuously from the nucleus to the end of the X-ray jet $\geq 4'$ from the nucleus. A slightly different view from the nucleus to knot B is shown in Figure 5, where the data in the 0.5–1.5 keV bandpass have been smoothed with a Gaussian ($\sigma = 0''.5$).

Our *Chandra* observations show that the X-ray jet consists of many knots of enhanced emission embedded within

diffuse emission. The diffuse emission extends continuously from the nuclear jet (knot NX1) into the northeast radio lobe beyond knot G. Each of the previously detected X-ray knots has considerable substructure when viewed at higher resolution. Using a wavelet decomposition source-detection algorithm to detect emission enhancements on angular scales of $0''.5$, $1''$, $2''$, and $4''$ (Vikhlinin et al. 1995), we find a total of 31 distinct knots or enhancements of X-ray emission embedded within the diffuse emission. Previous *Einstein* observations (Feigelson et al. 1981) detected seven distinct X-ray knots (labeled A to G), but subsequent *ROSAT* observations (Döbereiner et al. 1996) were unable to confirm knot D. Radio observations (Burns et al. 1983) showed that the inner knot (A) is actually composed of four sub-knots (A1 through A4). We refer to the inner $45''$ of the jet, which includes these compact radio knots, as the inner jet. Figure 6 contains a contour map of the unresolved diffuse emission from the jet with the contribution from the knots removed overplotted onto the adaptively smoothed image of the jet (Fig. 4). This contour map was created using a wavelet decomposition and retaining only emission on scales of $8''$ and larger.

As described in detail below, many of the radio and X-ray knots of the inner jet region do not exactly coincide, and all of the previously reported knots beyond the inner jet are

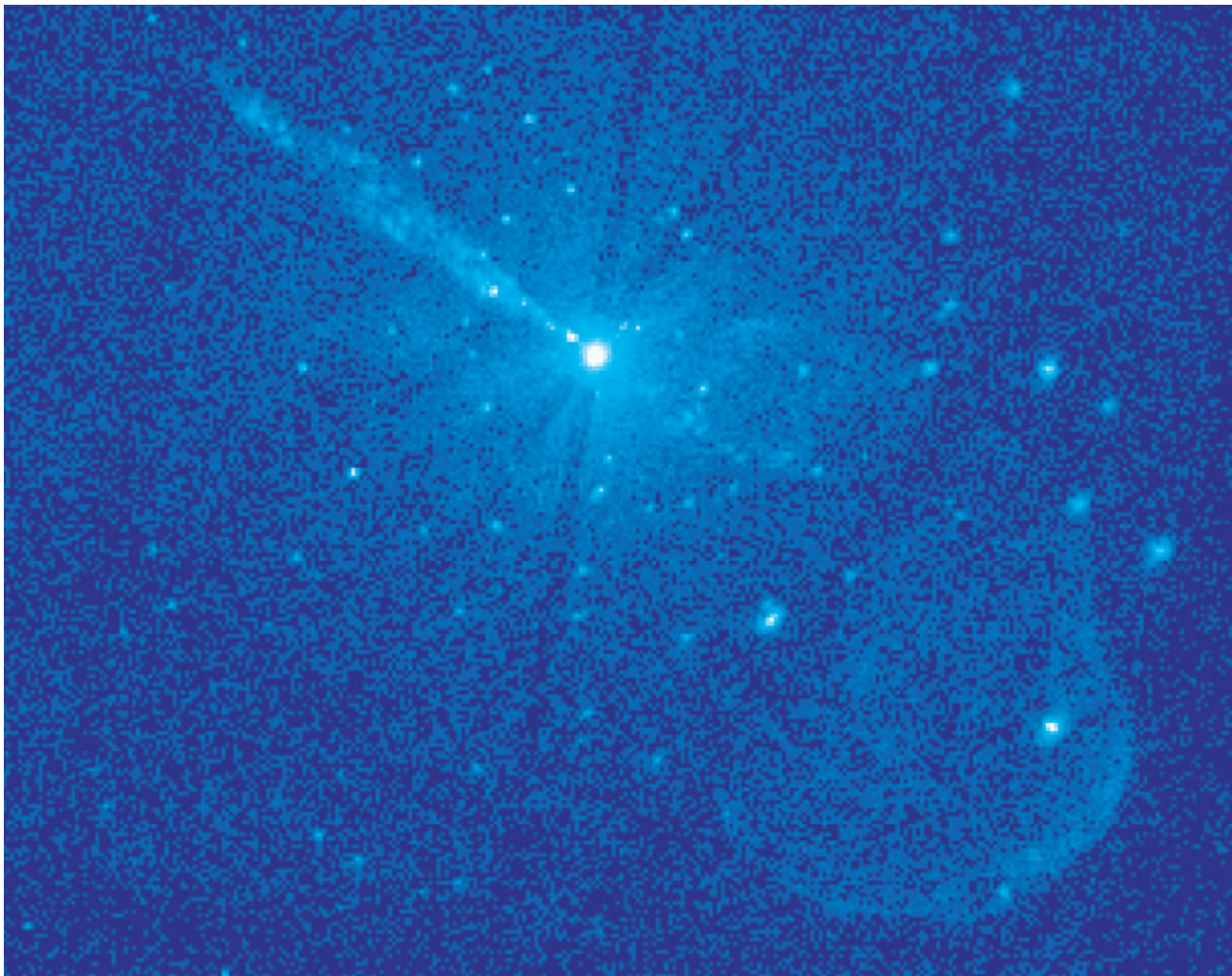


FIG. 2.—Raw X-ray image of Cen A in the 0.4–5 keV bandpass binned at $2''$ per pixel. The data from both observations have been co-added. The stripes radiating outward from the nucleus are the result of removing the frame-transfer streak in each observation due to out of time events from the nucleus. North is up and east is to the left. The image scale is approximately $10' \times 8'$.

actually composed of several smaller subknots. To avoid confusion, we will refer to the X-ray knots of the inner jet as AX1, AX2, etc., and knots beyond the inner jet as BX1, BX2, CX1, CX2, etc., depending on their location relative to the knots of Feigelson et al. (1981) to clearly distinguish them from the radio knots. The nomenclature of Burns et al. (1983) will be used when referring specifically to the radio knots. A summary of previously known radio and X-ray knots and their distances from the nucleus is contained in Table 1. When discussing X-ray jets, it is common to use the term *knot* to specifically describe the sites of enhanced emission where shocks may be accelerating the emitting particles. We have detected 31 sites of enhanced emission, but it is certainly not clear that they are all sites of shocks and particle acceleration, particularly the enhancements beyond knot B. For simplicity, however, we will use the term knot throughout this paper to describe these enhancements.

In the inner jet region, X-ray emission from the nuclear jet (radio knot N1) is clearly detected within $\sim 3''$ of the nucleus, and detectable X-ray emission is clearly present between the nuclear jet and the first bright radio/X-ray knot A1/AX1, as seen from Figure 5. The position of the first bright X-ray knot AX1 coincides (within our absolute uncertainty in astrometry $\sim 0''.5$) with radio knot A1 (see

TABLE 1
POSITIONS OF KNOTS

Knot ID	Distance from Nucleus (arcmin)
	Radio Knots
N1.....	0.05
A1.....	0.25
A2.....	0.33
A3.....	0.47
A4.....	0.53
B.....	1.12
E.....	1.88
F.....	2.43
X-Ray Knots	
A.....	0.23
B.....	1.00
C.....	1.25
E.....	1.85
F.....	2.27
G.....	3.40

NOTE.—Position of radio and X-ray knots of Cen A jet taken from Burns et al. 1983 and Feigelson et al. 1981, respectively.

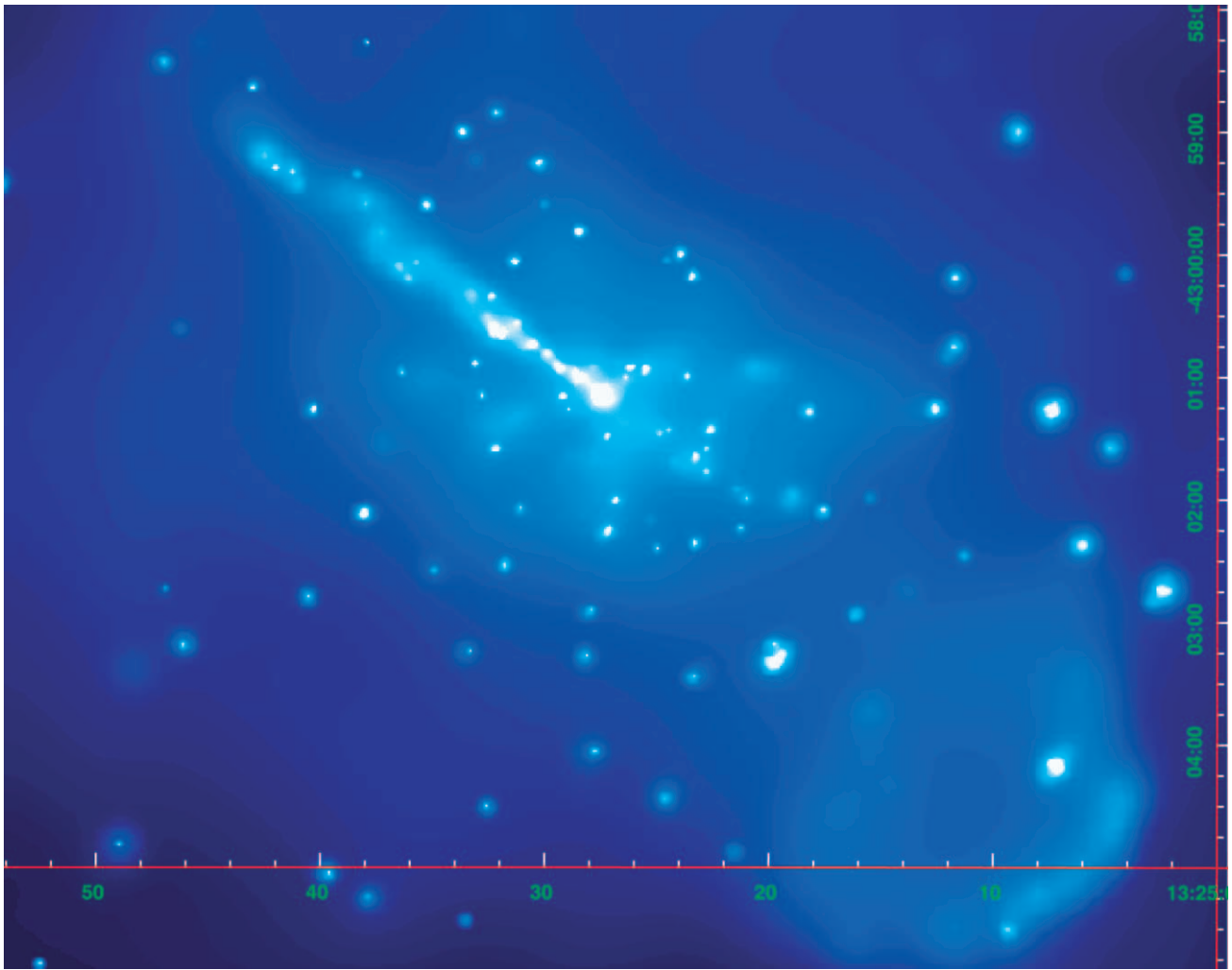


FIG. 3.—Adaptively smoothed, co-added, exposure-corrected X-ray image of Cen A in the 1–3 keV band. The nucleus is the bright source near the center of the field, and the jet extends to the northeast. North is up and east is left. Note the large number of point sources associated with the galaxy, the extended diffuse emission from the hot ISM, and emission from the southwest radio lobe.

below). Knot AX1 is clearly extended both along the jet and perpendicular to it. For reference, the PSF of the observation at the position of the nucleus (FWHM) is shown on the right-hand side of Figure 5. There is continuous diffuse emission and several X-ray knots between radio knots A1 and B, and there is a kink or bend in the jet direction between knots AX2 and AX3. An image of the X-ray contours in the 0.4–1.5 keV bandpass overlaid onto an optical (*HST*) image of Cen A is shown in Figure 7. The region of low X-ray surface brightness between knots AX5 and AX6 corresponds with dark dust bands in the optical. The jet appears to widen dramatically before knot B just as it emerges from behind the dust lane, although it appears to remain collimated. Beyond knot B, the jet is composed of both knots and diffuse emission. The width of the jet is approximately constant out to knot E (~ 2.5 from the nucleus), where the jet apparently begins to narrow (see Fig. 3), although whether this is a real feature or just the result of a decrease in the X-ray surface brightness is not clear.

Variable absorption in the inner jet region might have an effect on the observed X-ray structure. The optical extinction, A_V , in the inner jet region varies between 0.5 and 3.0 mag (Schreier et al. 1996). Adopting a standard Galactic

gas-to-dust ratio, this corresponds to an X-ray column of $(0.9\text{--}5.6) \times 10^{21} \text{ cm}^{-2}$ (Smith & Dwek 1998). For a power-law spectrum with photon index of 2.2, this variation in N_H would correspond to a variation of a factor of ~ 2 in count rate in ACIS-I in the 0.4–2.5 keV bandpass of the ACIS-I, although in the region from the core to AX4 (before the dark dust lanes are encountered), the positional variations in X-ray count rate contributed by the absorption are expected to be less than 10%. The actual relationship between the X-ray emission from the jet and any intervening absorbing material is probably more complex for two reasons. First, the angle of the jet to the line of sight is poorly constrained, so the geometric relationship of the jet relative to the gas associated with the optically obscuring dust is by no means clear. Second, the X-ray spectral fitting (described below) suggests that the absorbing column of the brightest knots of the inner jet (AX1–AX4) is considerably larger ($N_H \sim 6 \times 10^{21} \text{ cm}^{-2}$) than one would expect based on the extinction map of Schreier et al. (1996). In fact, this X-ray column density is at the high end of the range inferred from A_V over most or all of the inner jet. We note that the morphological features of the inner jet seen in the broadband X-ray image are still present when X-rays in the 1–3 keV

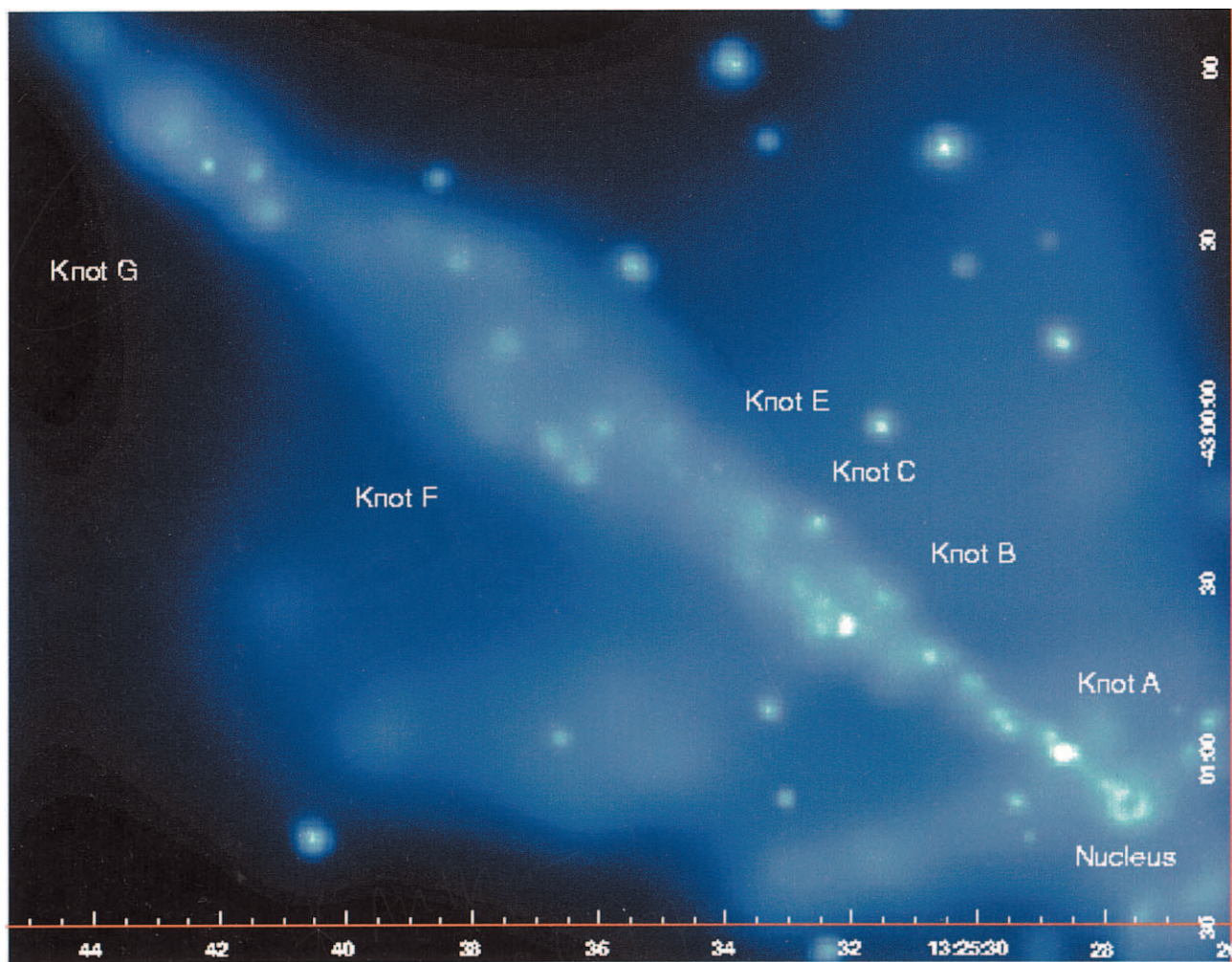


FIG. 4.—Adaptively smoothed, co-added image in the 0.4–2.5 keV bandpass of the Cen A jet. North is up and east is to the left. The unusual donut shape of the nucleus to the southwest is caused by pileup in the ACIS detector. Each of the knots previously detected by *Einstein* and *ROSAT* has been clearly resolved into several distinct subknots and enhancements embedded within diffuse extended emission. The knots and enhancements have been labeled in the same manner as Table 2.

band only are selected, so the appearance of the inner jet is probably not significantly distorted because of variable absorption.

To determine which of these knots are extended and which are pointlike and may therefore be XRBs unrelated to the jet, we have simulated point sources at five positions separated by $1'$ along the jet starting at the nucleus using MARX. We used only data from the first (OBSID 00316) observation since the jet is closer to the best focus, and co-adding the second data set at a different roll angle would add considerable systematic uncertainty. The ratio of the number of counts within a $1''$ radius circle to the number of counts within a $1''$ – $2''$ annular ring was determined for each of these simulated point sources. A third-order polynomial was fitted to this ratio as a function of distance from the nucleus in order to estimate this ratio at an arbitrary position along the jet. The measured ratio for each of the detected enhancements was then compared to the simulated ratio. If the measured ratio is less than 3σ below the simulated ratio, the enhancement is considered a point source. On the basis of this test, we find that three of the enhancements are consistent with point sources (see Table 2). The normalized surface brightness profiles of the two brightest

knots, AX1 and BX2, and the MARX simulations of the PSFs at the locations of those knots are plotted in Figure 8. We have evaluated this procedure by testing other sources located near the jet but clearly outside the diffuse emission, and we find that four of the five sources are consistent with being point sources. The fifth source is obviously distorted and, by visual inspection alone, it is clear that it should not be considered a point source. The position, background-subtracted count rate, and luminosity of each knot are given in Table 2. Based on the radial surface-density distribution of X-ray point sources in Cen A (Kraft et al. 2001), we expect three of the knots or sources to be X-ray binaries within Cen A but unrelated to the jet. We conclude that the remaining knots are features of the jet structure that are resolved by *Chandra*.

The X-ray morphology of the jet is clearly more complex when observed at higher resolution. It is therefore reasonable to expect that there may be even more complex structure at smaller spatial scales that can only be resolved at higher resolution. To estimate what fraction of the remaining unresolved emission of the jet could result from a large number of unresolved lower luminosity knots, we created the luminosity function (LF) for the jet knots shown in

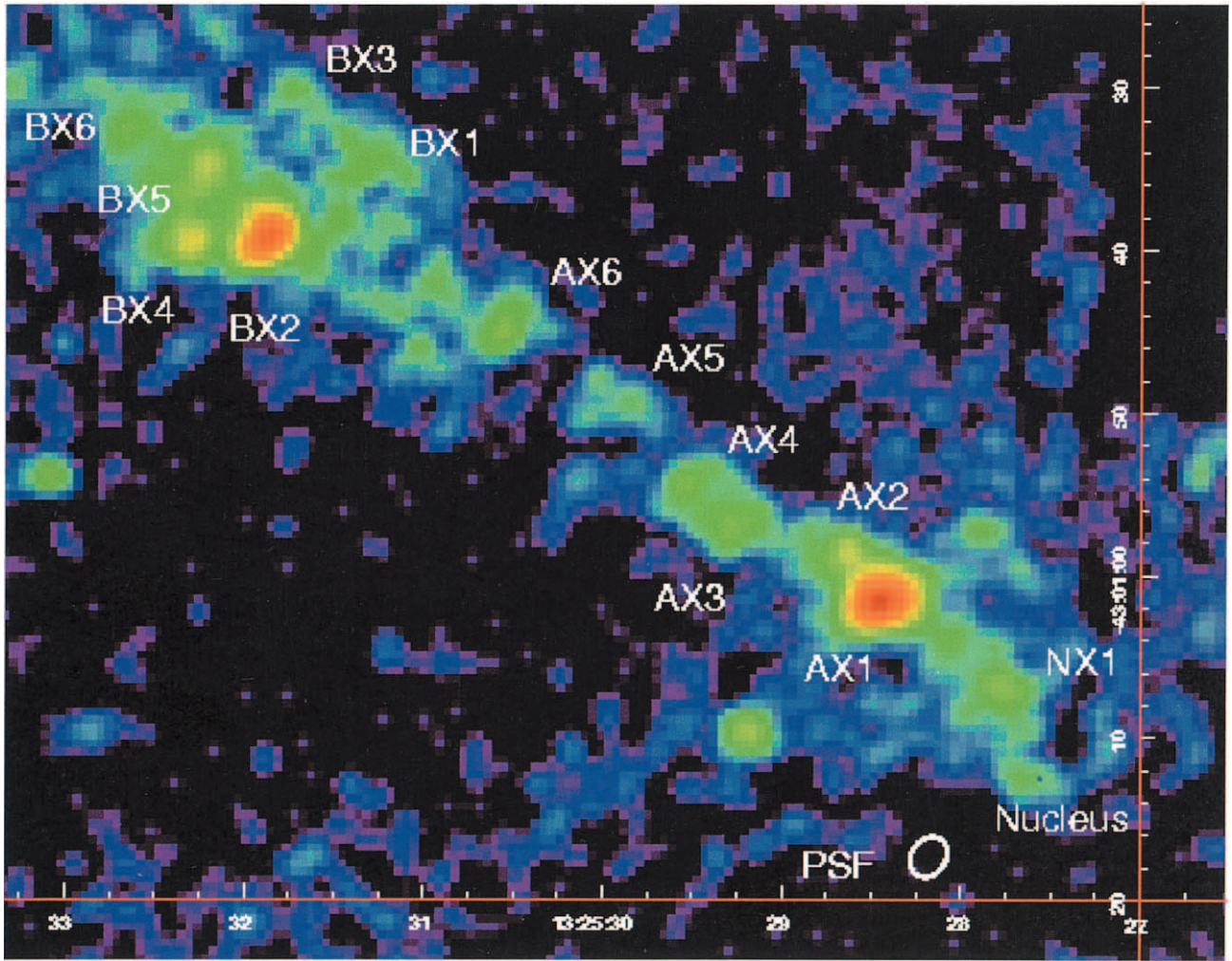


FIG. 5.—Image of inner jet and radio knot B region of Cen A in the 0.4–1.5 keV bandpass. This image contains data from only one (OBSID 00316) of the observations and is in a softer band than Fig. 4 to suppress the heavily absorbed nucleus. The data have been smoothed by a $0''.5$ (rms) Gaussian. The X-ray knots have been labeled in the same manner as in Table 2. The PSF (FWHM smoothed by a $0''.5$ [rms] Gaussian) to match the data at 1.5 keV at the position of the nucleus based on MARX simulations (see text for full discussion) is shown below the nucleus.

Figure 9. The luminosity of the knots is taken from Table 2. We assume a power-law spectrum with photon index 2.3 and $N_{\text{H}} = 1.7 \times 10^{21} \text{ cm}^{-2}$. The knots of the inner jet (NX1 and AX1–AX6) were excluded because the variable absorption makes determination of the unabsorbed luminosity more uncertain. The knots we identified as point sources (CX1 and EX1) have been excluded as well. The limiting sensitivity for this analysis is somewhat uncertain because of source confusion and depends on the distribution of luminosity and spatial extent among the knots. A detailed computation of the limiting sensitivity for detection of knots in the jet would require a Monte Carlo simulation and is beyond the scope of this paper. We note that the limiting sensitivity away from the jet region for which point-source detection is complete and unbiased is $\sim 3 \times 10^{37} \text{ ergs s}^{-1}$ (Kraft et al. 2001). Source confusion and source extent will increase this value, but this increase is offset somewhat because we co-added the two observations for this analysis. For simplicity, we choose the limiting luminosity for knot detection, $L_{\text{sens}} = 3 \times 10^{37} \text{ ergs s}^{-1}$, the same as for point-source detection. This is approximately the luminosity at which the LF begins to flatten (see Fig. 9). The results below are not sensitive to this choice.

We fit a power law to the knot LF for knots with $L_{\text{X}} > 3 \times 10^{37} \text{ ergs s}^{-1}$ to quantify the distribution of knot luminosities. We parameterize the LF as

$$N(> L) = N_0 \left(\frac{L}{L_0} \right)^{-\alpha},$$

where N_0 is the normalization at $L_0 = 10^{39} \text{ ergs s}^{-1}$. The best-fit parameters are $\alpha = 1.1$ and $N_0 = 0.28$. If this distribution is extended to some minimum luminosity, L_{min} , the integrated X-ray flux from the jet (using the best-fit parameters) between L_{min} and L_{max} (the luminosity of the brightest detected knot) is given by

$$L_T = 3.09 L_0 \left[\left(\frac{L_{\text{min}}}{L_0} \right)^{-0.1} - \left(\frac{L_{\text{max}}}{L_0} \right)^{-0.1} \right].$$

The total luminosity of the jet in a region $195''$ long and $30''$ wide beginning at a distance of $45''$ from the nucleus containing all the knots in the LF is $3.59 \times 10^{39} \text{ ergs s}^{-1}$. The integrated luminosity of the detected knots in this region is $1.23 \times 10^{39} \text{ ergs s}^{-1}$. The remainder of the emission of the jet can be entirely accounted for if $L_{\text{min}} = 3 \times 10^{35} \text{ ergs s}^{-1}$,

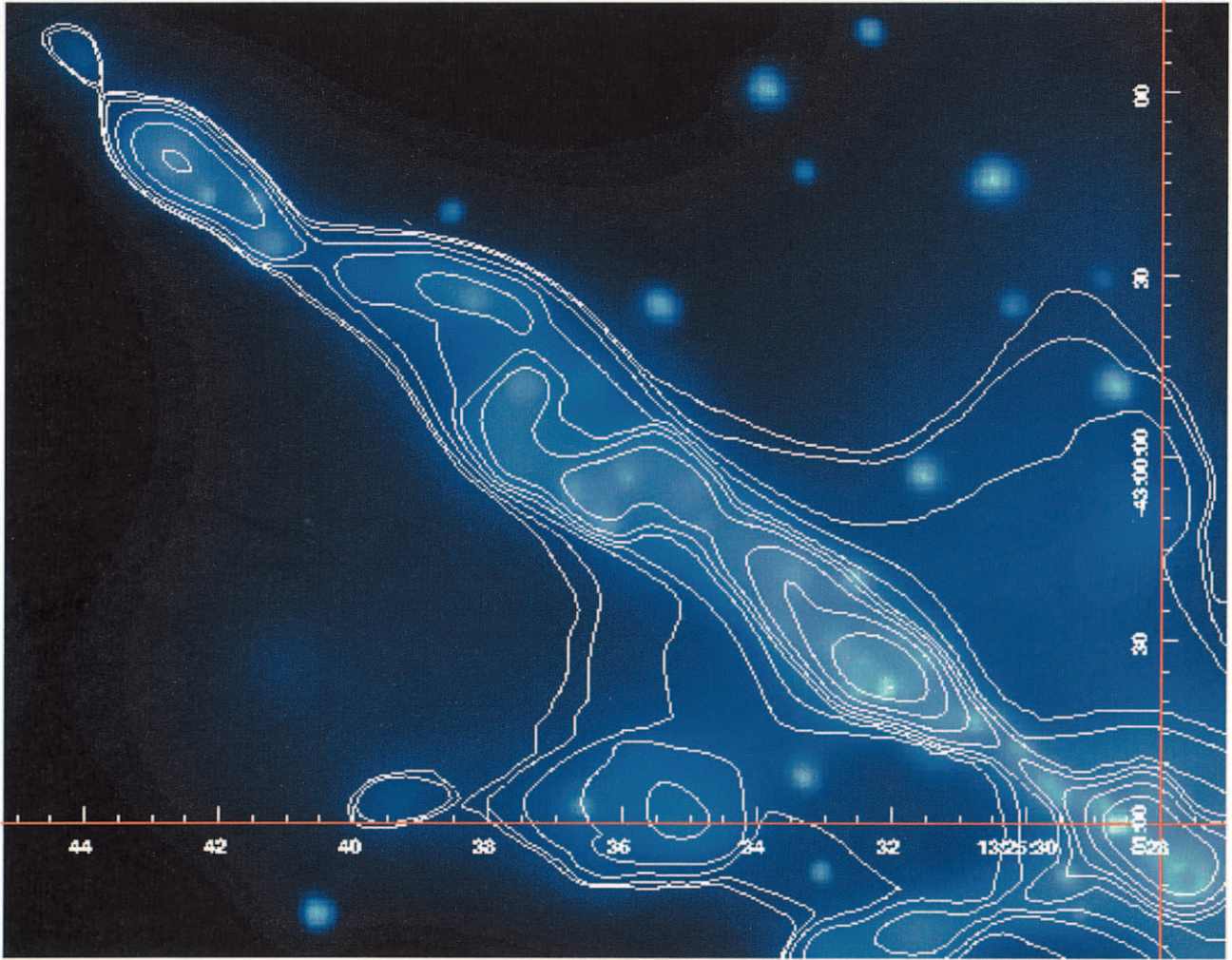


FIG. 6.—Contour plot of the unresolved, diffuse emission of the X-ray jet in the 0.4–2.5 keV band overlaid onto the adaptively smoothed image in the same band (Fig. 4). The contours were created using a wavelet decomposition, retaining only emission on scales of $8''$ or larger. The contours correspond to surface brightnesses of 0.45, 0.51, 0.70, 1.02, 1.46, 2.03, 2.72, 3.55, 4.50, and 5.58×10^{-5} counts arcsec $^{-2}$ s $^{-1}$ above background.

assuming there is no break in the index of the LF below L_{sens} . The total number of knots at this minimum luminosity $N(> L_{\text{min}})$ is ~ 1700 . Based on this simple analysis, it is possible that the unresolved diffuse emission of the jet actually consists of many lower luminosity, and perhaps smaller scale, knots. Each of the detected knots may, in fact, actually consist of several unresolved lower luminosity knots.

3.2. Comparison of X-Ray and Radio Morphology

Figure 10 contains an adaptively smoothed X-ray image of the jet with 3.6 cm radio contours overlaid. The inner jet region, from the nucleus to just beyond knot B, is shown in Figure 11 with the 3.6 cm radio contours overlaid. The resolution of radio data is $3''.39$ (R.A.) \times $4''.70$ (decl.) (FWHM) in Figure 10 and $0''.23$ (R.A.) \times $0''.99$ (decl.) (FWHM) in Figure 11. The approximate positions of the X-ray and radio knots are labeled in Figure 11 above and below the jet, respectively. Within the $\sim 0''.5$ absolute positional resolution of the X-ray image, the position of radio knot A1 agrees with that of the first bright X-ray knot AX1. We detect weak X-ray emission between the nuclear jet (NX1) and this first

bright X-ray knot coincident with previously observed radio emission (Marconi et al. 2000). Farther along the jet, however, there is a noticeable difference between the peaks in the X-ray emission and the radio emission. At knot B, the peak of the X-ray emission is $5''$ (~ 80 pc) closer to the nucleus than the peak of the radio emission. The ratio of X-ray to radio flux for knots AX1/A1 and BX2/B is considerably higher than for the rest of the jet. Such an anomalous brightness at one or two knots in the jets of several other FR I radio galaxies has recently been reported (Hardcastle et al. 2001) and may be a fundamental characteristic of such jets.

Although morphological differences between the X-ray and radio emission are significant both along the jet and perpendicular to it, these can be seen more clearly by viewing the jet in projection. Figure 12 shows the intensity profile of the jet in a projection $24''$ wide along position angle 55° in both the X-ray (0.4–1.8 keV to suppress the mirror-scattered nuclear contribution) and radio (3.6 cm). This projection extends $100''$ from the nucleus along the jet to a region just beyond knot B. No background has been subtracted from the X-ray data, but, as can be seen from the gaps between the knots, the background is small in this projection. The radio positions of the knots (A1–A4 and B;

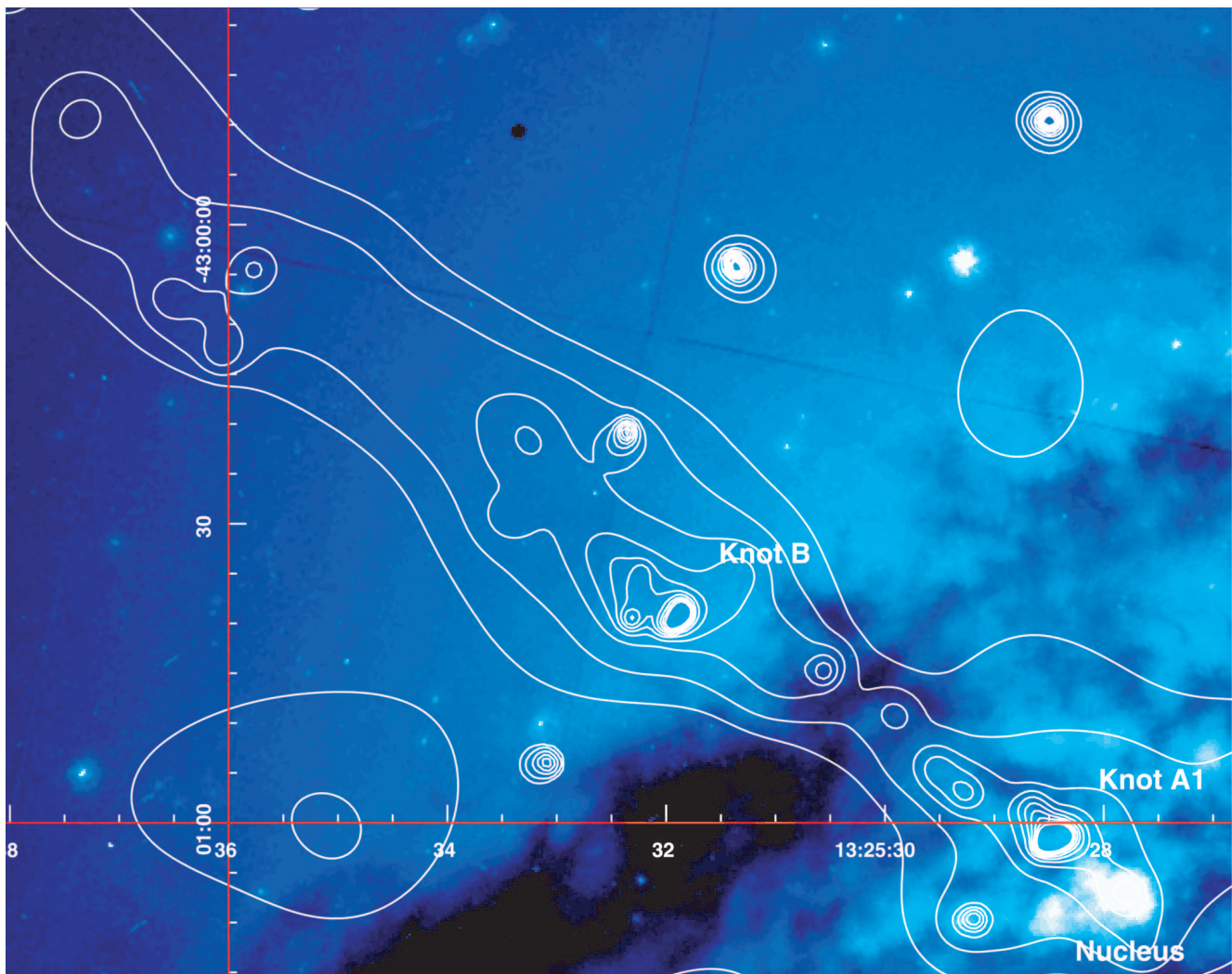


FIG. 7.—Adaptively smoothed X-ray contours of the jet in the 0.5–1.5 keV bandpass overlaid on a 350 s *HST*/WFPC (F675W filter central wavelength 6731 Å) image taken from the *HST* archive. The X-ray contours correspond to surface brightnesses of 9.22, 16.3, 37.1, 72.2, 121, 184, 261, 352, 457, and 576×10^{-6} counts $\text{s}^{-1} \text{arcsec}^{-2}$. The background rate at a region adjacent to the end of the jet (i.e., beyond any significant contribution from the hot ISM of the galaxy) is 2.07×10^{-6} counts $\text{s}^{-1} \text{arcsec}^{-2}$.

Burns et al. 1983) of the inner jet have been labeled. Differences and offsets between the X-ray and radio emission of the jet are apparent. There is a small difference between the radio and X-ray peaks at knot A1/AX1, but this difference is consistent with our $\sim 0''.5$ uncertainty on the absolute alignment of the X-ray data and centroiding the position of the X-ray nucleus because of the pileup. Beyond knot A1, however, the morphological differences are significant. The second (AX2) and third (AX3) X-ray knots of the inner jet lie approximately $2''.5$ (~ 40 pc) closer to the nucleus than the second (A2) and third (A3) radio knots, whereas the fourth knot (AX4) lies approximately $5''$ farther from the nucleus than the fourth (A4) radio knot. Knot AX6 (knot AX in Kraft et al. 2000) coincides with a small peak in the radio emission. The region between the fourth radio knot (A4) of the inner jet and radio knot B is crossed by several dark optical bands (see Fig. 7). The radio position of the nuclear jet is several arcseconds from the nucleus (Burns et al. 1983) and is labeled N1. We detect a significant X-ray enhancement at the position of this nuclear jet (labeled NX1) and continuous emission from this knot to X-ray/radio knot A1. The X-ray emission from knot B is com-

posed of emission from one bright knot, which lies $\sim 5''$ closer to the nucleus than the radio peak, and five fainter knots surrounded by diffuse emission.

These high-resolution *Chandra* observations permit us to measure the transverse width of the X-ray jet as a function of distance from the nucleus. As can be seen from Figure 4, the jet progressively widens along its length, and several bends or turns are visible in the inner jet region between the nucleus and knot B. In the inner jet region, the width of the jet is only marginally resolved in our data. As described above, we used MARX simulations (Wise, Huenemoerder, & Davis 1997) to model the PSF of the observation at 1.5 keV for the location of the inner jet in the first observation (OBSID 00316). We used only one observation for this analysis to avoid uncertainties that would be introduced by combining the PSFs of two observations at different roll angles and off-axis positions. In the inner jet region, we estimated the width of the jet perpendicular to the direction of propagation according to

$$\sigma_{\text{knot}} = \sqrt{\sigma_{\text{obs}}^2 - \sigma_{\text{PSF}}^2}, \quad (1)$$

TABLE 2
SUMMARY OF KNOTS AND ENHANCEMENTS DETECTED IN THE CEN A JET

Knot	ID	Distance (arcmin)	Angle (deg)	R.A. (J2000.0)	Decl. (J2000.0)	Counts	Net Rate ($\times 10^3$ counts s^{-1})	L_x
1.....	NX1	0.09	48.58	13 25 27.88	-43 01 06.4	198	1.44 ± 0.24	$1.51E+38$
2.....	AX1	0.25	52.94	13 25 28.65	-43 01 00.1	1303	17.66 ± 0.50	$1.84E+39$
3.....	AX2	0.30	50.49	13 25 28.84	-43 00 56.9	234	2.93 ± 0.22	$3.07E+38$
4.....	AX3	0.42	57.70	13 25 29.51	-43 00 55.9	201	2.71 ± 0.20	$2.84E+38$
5.....	AX4	0.47	55.05	13 25 29.70	-43 00 53.8	166	2.22 ± 0.18	$2.23E+38$
6.....	AX5 ^a	0.59	52.89	13 25 30.09	-43 00 48.2	94	1.27 ± 0.14	$1.33E+38$
7.....	AX6	0.71	52.93	13 25 30.76	-43 00 43.6	209	2.86 ± 0.20	$2.99E+38$
8.....	BX1	0.94	49.97	13 25 31.50	-43 00 33.4	155	2.10 ± 0.17	$7.40E+39$
9.....	BX2	0.96	57.19	13 25 32.04	-43 00 38.0	830	11.39 ± 0.40	$4.01E+38$
10.....	BX3	1.03	51.45	13 25 31.85	-43 00 29.2	71	0.90 ± 0.12	$3.16E+39$
11.....	BX4	1.03	60.28	13 25 32.52	-43 00 38.0	242	3.26 ± 0.22	$1.15E+38$
12.....	BX5	1.06	56.00	13 25 32.43	-43 00 33.4	193	2.56 ± 0.20	$9.01E+37$
13.....	CX1 ^a	1.14	56.71	13 25 32.88	-43 00 31.0	131	1.67 ± 0.16	$5.89E+37$
14.....	CX2	1.23	47.43	13 25 32.56	-43 00 19.4	174	2.27 ± 0.19	$7.98E+37$
15.....	CX3	1.29	58.28	13 25 33.74	-43 00 28.5	57	0.72 ± 0.11	$2.53E+37$
16.....	CX4	1.35	53.16	13 25 33.52	-43 00 20.1	93	1.23 ± 0.14	$4.33E+37$
17.....	EX1 ^a	1.54	50.60	13 25 34.13	-43 00 10.2	40	0.47 ± 0.09	$1.66E+37$
18.....	EX2	1.63	53.79	13 25 34.80	-43 00 10.9	39	0.50 ± 0.09	$1.75E+37$
19.....	EX3	1.73	51.15	13 25 34.86	-43 00 04.3	49	0.57 ± 0.10	$2.00E+37$
20.....	FX1	1.85	58.82	13 25 36.27	-43 00 11.6	80	1.05 ± 0.13	$3.70E+37$
21.....	FX2	1.87	54.26	13 25 35.95	-43 00 03.2	86	1.15 ± 0.13	$4.04E+37$
22.....	FX3	1.96	58.01	13 25 36.72	-43 00 06.7	77	1.05 ± 0.12	$3.70E+37$
23.....	FX4	2.03	57.56	13 25 36.98	-42 00 03.9	44	0.55 ± 0.10	$1.95E+37$
24.....	FX5	2.15	58.59	13 25 37.65	-43 00 01.8	37	0.50 ± 0.09	$1.75E+37$
25.....	FX6	2.24	53.32	13 25 37.46	-42 59 49.1	69	0.91 ± 0.12	$3.21E+37$
26.....	FX7	2.51	51.09	13 25 38.32	-42 59 34.7	58	0.77 ± 0.11	$2.73E+37$
27.....	GX1	3.02	55.17	13 25 41.17	-42 59 25.6	57	0.77 ± 0.11	$2.73E+37$
28.....	GX2	3.13	53.75	13 25 41.43	-42 59 18.2	65	0.87 ± 0.11	$3.07E+37$
29.....	GX3	3.26	55.05	13 25 42.23	-42 59 17.2	97	1.32 ± 0.14	$4.67E+37$
30.....	GX4	3.40	54.53	13 25 42.78	-42 59 10.8	65	0.90 ± 0.11	$3.16E+37$
31.....	GX5	3.75	53.27	13 25 44.12	-42 58 55.0	14	0.19 ± 0.05	$6.81E+36$

NOTE.—Units of right ascension are hours, minutes, and seconds, and units of declination are degrees, arcminutes, and arcseconds. Distance is the angular distance from the nucleus in arcminutes, angle is the position angle from the nucleus to the knots measured east from north, counts are the source counts in a $3''.5$ (inner jet: knots NX1 and AX1–AX6) or $4''$ radius circle around each feature in the 0.4–2.5 keV band (not background subtracted), rate is the background-subtracted rate and statistical uncertainty, and luminosity is given in the 0.1–10 keV band (unabsorbed) assuming a power-law spectrum of photon index 2.5 and $N_H = 7.2 \times 10^{21}$ cm $^{-2}$ (inner jet: knots AX1–AX6) or photon index 2.3 and $N_H = 1.7 \times 10^{21}$ cm $^{-2}$ (all other knots and enhancements) computed using HEASARC PIMMS. The background was estimated from a region extending radially from the nucleus adjacent to the jet.

^a Enhancements consistent with point sources as defined by the encircled energy test described in the text; they are therefore possibly XRBs unrelated to the jet.

where σ_{knot} is the width of the knot (FWHM), σ_{obs} is the observed width (FWHM) of the knot, and σ_{PSF} is the width of the PSF (FWHM). Beyond the inner jet, the transverse width of the jet is clearly resolved and can be measured directly.

The width of the X-ray jet as a function of distance from the nucleus is plotted in Figure 13. For comparison, the FWHM of the individual features in the jet taken from earlier radio measurements (taken from Fig. 4 and Table 2 of Burns et al. 1983) at two angular resolutions are also plotted. The width measured from our more sensitive 3.6 cm radio data shown in Figure 10 is plotted as the solid curve. We note that these are two somewhat different definitions of width. Burns et al. (1983) define the radio width of the jet as the second moment of the brightness distribution. We have chosen the surface brightness boundary of the jet as the definition of width for the 3.6 cm data shown as the solid curve in Figure 10. This difference permits a more straightforward comparison with our X-ray data, since we have chosen two

similar definitions of the width for our X-ray analysis. It is appropriate to compare the radio widths of Burns et al. (1983) with our measurements of the X-ray widths in the inner jet region and the 3.6 cm radio widths with the X-ray widths beyond the inner jet region. As can be seen from Figure 10, the X-ray width of the jet at knot AX1 is marginally smaller than the radio width. Beyond knot AX1, however, the X-ray jet is definitively narrower than the radio jet. It is not clear whether this is a real feature or an instrumental artifact related to the low X-ray surface brightness at the edge of the jet as it becomes undetectable above the emission from the hot ISM. If this difference in width is a real feature of the jet, it implies that the higher energy X-ray-emitting plasma is confined in a narrower channel than the radio-emitting plasma.

We also made projections of the data along a position angle of 55° in two different energy bands, 0.4–1.5 and 1.5–5.0 keV, to investigate whether there are differences in the width of the jet in the two X-ray bands, which would sup-

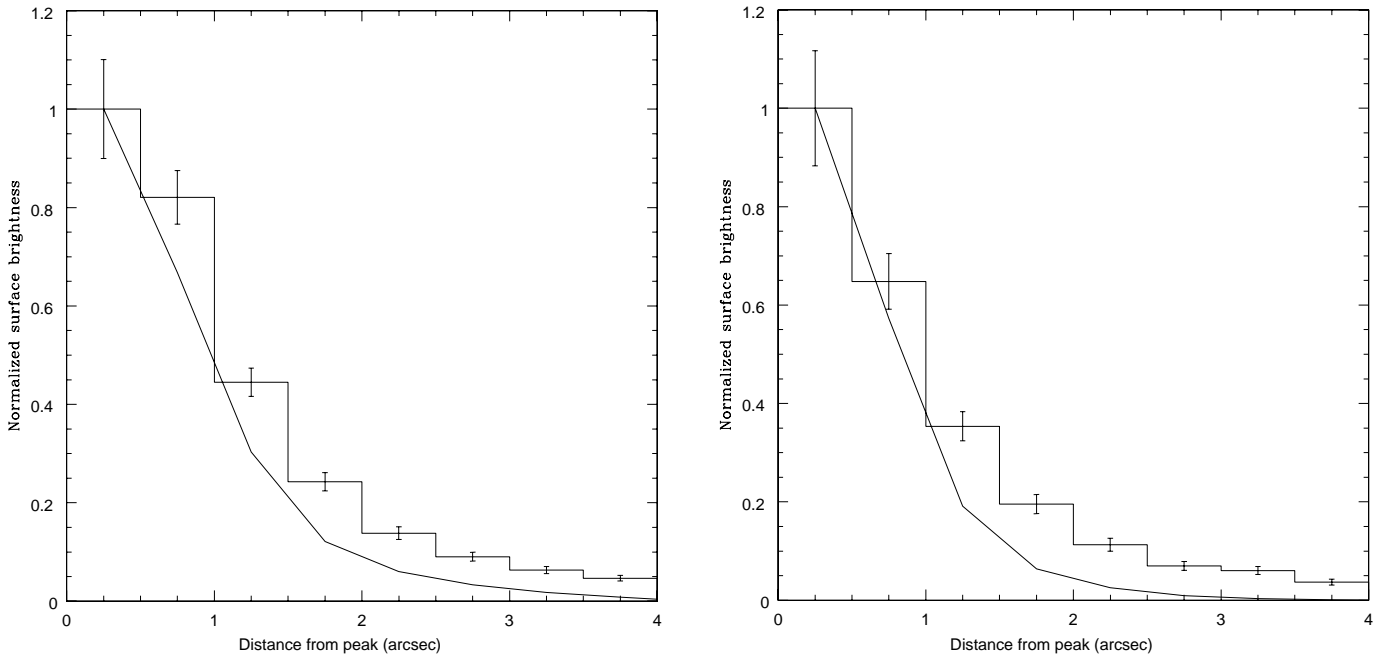


FIG. 8.—Surface brightness (normalized counts arcsec⁻² s⁻¹) distributions of X-ray knots AX1 (*left*) and BX2 (*right*) in 0".5 bins within a 4" radius of the knot peak in the 0.4–2.5 keV band. The surface brightness distributions of the MARX simulated PSFs at the locations of the knots at 1.5 keV are shown as the continuous curves. The data have been normalized to have the unity surface brightness in the first bin. Error bars are the result of counting statistics only.

port the idea that the most energetic particles are constrained within a smaller channel of the jet. Four regions of the jet were projected: the inner jet between, but not including, knot AX1 and knot B, knot B, and two regions beyond knot B. The regions are summarized in Table 3. Figure 14 contains the first two of these projections; the other two are similar. The data from the two observations have been co-

added but not exposure corrected. We find no statistically significant difference in the width of the jet in the two bands at any position along the jet, implying that the particles responsible for the emission in the two bands are homogeneously mixed. This result also suggests that variable absorption is not significant in modifying the transverse morphology of the jet.

Two knots of radio emission in the southwest radio lobe (Clarke, Burns, & Norman 1992) could be related to a counterjet. Similarly, several pointlike sources of X-ray emission have been detected in both the HRC image (Kraft et al. 2000) and the ACIS observations presented here. There are five bright X-ray points that are approximately colinear with the nucleus and the forward jet, suggestive of a counterjet. Several of these points are near (~5") but not coincident with the radio knots. The two radio knots are not colinear with the nucleus and forward jet. X-ray spectra of these unresolved sources are not significantly different from that of the population of X-ray binaries (Kraft et al. 2001). It is possible that the emission from these unresolved X-ray sources may be related to a nonthermal process originating

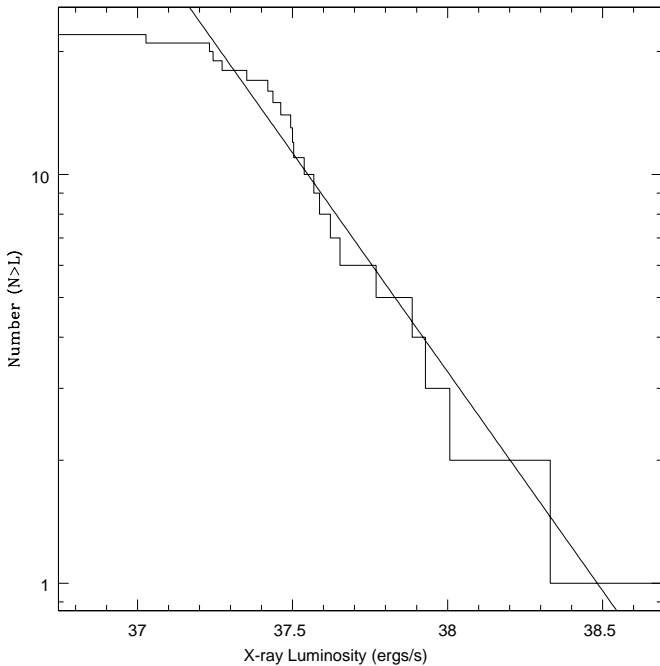


FIG. 9.—Luminosity function of knots in X-ray jet, excluding the knots of the inner jet and those identified as point sources. The X-ray luminosity is the unabsorbed luminosity in the 0.1–10 keV band assuming a power-law spectrum with photon index 2.3 and $N_H = 1.7 \times 10^{21}$ cm⁻². The best-fit power-law model for $L_X > 3 \times 10^{37}$ ergs s⁻¹ is also shown.

TABLE 3
SUMMARY OF PROJECTED REGIONS OF THE CEN A JET

Projection	Inner Radius (arcsec)	Outer Radius (arcsec)	Approximate Location
1.....	20.7	48.2	Knots AX1–AX4
2.....	48.2	76.8	Knot B
3.....	76.8	124.5	Knots C and E
4.....	124.5	214.9	Knots F and G

NOTE.—We have determined the width of the jet in projection (rotated through position angle 55°) in two energy bands (0.4–1.5 and 1.5–5 keV) for each of these regions. The projections of the first two regions are shown in Fig. 14. We find that there is no difference in the width of the jet in the two energy bands in these four regions.

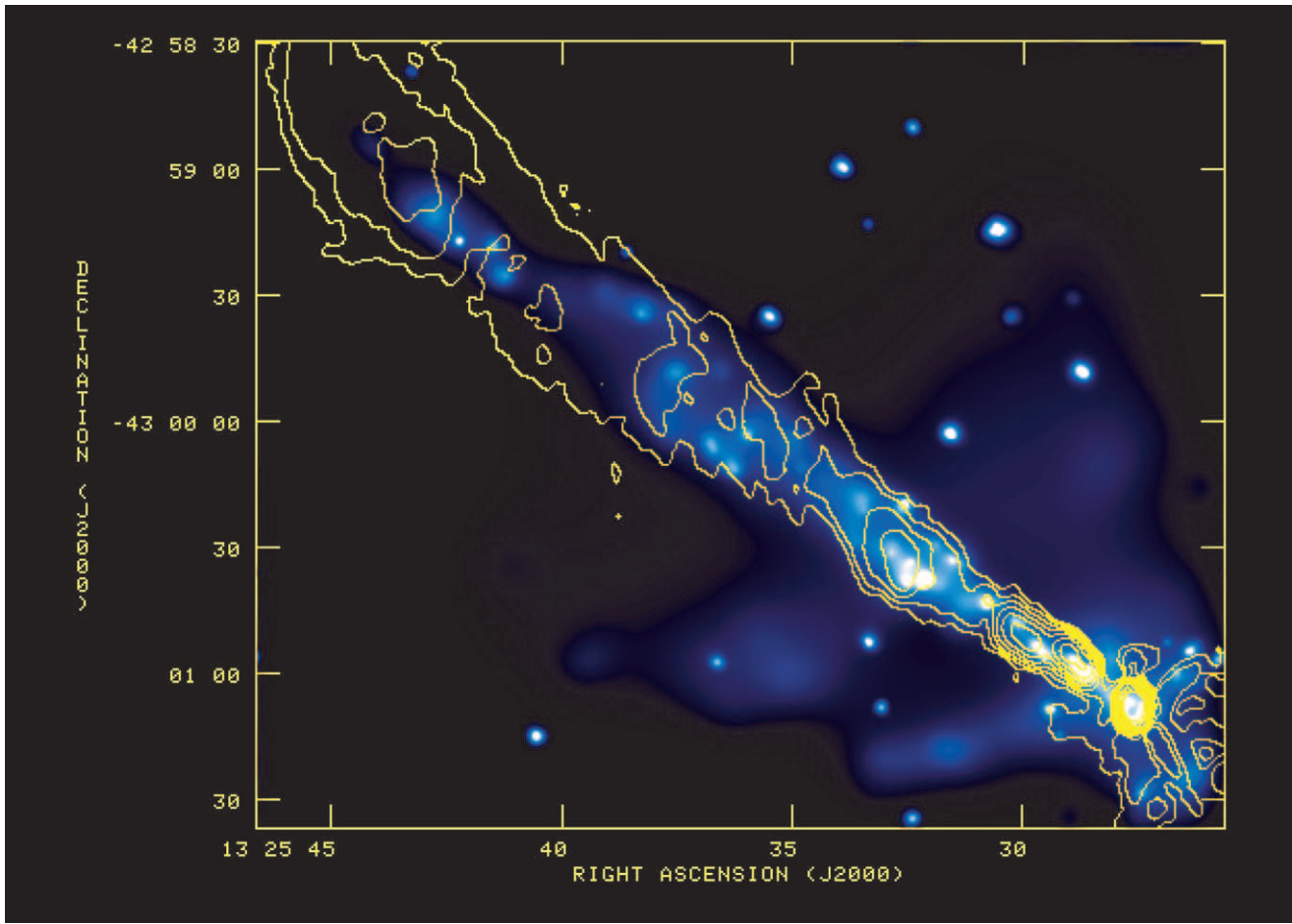


FIG. 10.—Adaptively smoothed, co-added X-ray image in the 0.4–2.5 keV bandpass of the jet in Cen A with 3.6 cm radio contours overlaid. North is up and east is to the left. The radio beam is $3''.39$ (R.A.) \times $4''.70$ (decl.).

in a collimated outflow from the nucleus, but without additional evidence, we conclude that these sources are XRBs within Cen A unrelated to a counterjet.

3.3. Spectral Analysis

We derived spectral parameters for four regions of the jet. These regions are knot A1, knot B, the knots between A1 and B, and all of the emission beyond knot B to the edge of the X-ray jet. It was not possible to simply combine the data from the two observations for spectral analysis for two reasons. First, the focal plane temperature at the time of the first observation was -110°C , but it had been changed to -120°C by the time of the second. Second, even though the entire jet was placed on one chip for both observations, the jet spans different parts of the chips for each one. Given the variation in spectral response across output nodes and across a chip due to radiation damage, it was necessary to generate response matrices for each observation and fit data from both observations simultaneously. For the last two regions, a response matrix appropriate for the center of the given region was used. None of the regions crosses the output node boundaries.

We have fitted absorbed power law, Raymond-Smith with variable abundance, and thermal bremsstrahlung models to the spectra in the 0.4–4.5 keV band. All three models produce acceptable fits, and there is no statistical reason to

choose one over the other. The best-fit temperatures of the Raymond-Smith and thermal bremsstrahlung models range between 3 and 5 keV with large uncertainty. The abundance in the Raymond-Smith fits is low (~ 0.1 solar but statistically consistent with zero) and poorly constrained. Such a high-temperature, low-abundance plasma has no spectral features or emission lines that can be resolved at the resolution of the ACIS-I instrument and is indistinguishable from the absorbed power-law model when fitted over a restricted energy band. Although our data do not rule out a thermal model, we reject them on physical grounds as described below and consider only the absorbed power-law model further.

The spectra and best-fit power law for knots A1 and B are shown in Figure 15, and the parameters of all of the fits of the absorbed power-law model are summarized in Table 4. Note that in all cases the best-fit absorbing column is larger than the Galactic value of $7 \times 10^{20} \text{ cm}^{-2}$ (Stark et al. 1992), implying considerable absorption within Cen A. This is not surprising for the inner jet region where the jet crosses the dust lane. As described above, the best-fit column density for the two inner jet regions is at the high end of the range suggested by A_V . Significant amounts of neutral hydrogen ($N_{\text{H}} \sim \text{few} \times 10^{20} \text{ cm}^{-2}$) have been detected in the vicinity of the jet beyond knot B out to knot F (Schiminovich et al. 1994), implying that perhaps the jet is behind much of this

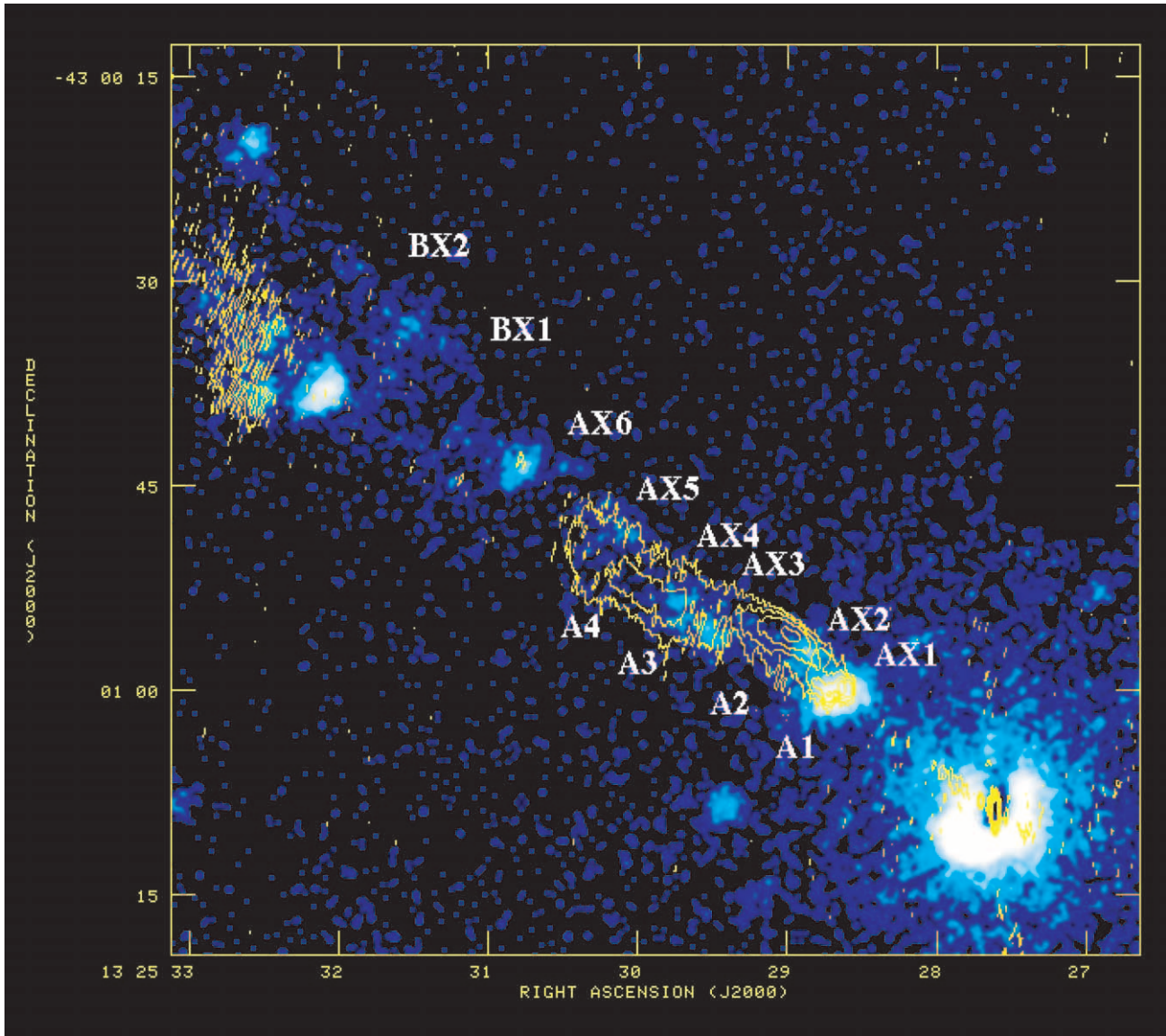


FIG. 11.—Smoothed (Gaussian: FWHM = 0.5) X-ray image in the 0.4–5 keV bandpass of the inner jet in Cen A with 3.6 cm radio contours overlaid. North is up and east is to the left. The radio beam is 0.23 (R.A.) \times 0.99 (decl.).

absorbing material. The best-fit index for the emission beyond knot B is similar to that of the brighter knots of the inner jet. The flux from this region of the jet is dominated ($\sim 75\%$) by the diffuse unresolved component. This spectral

similarity between the knots of the inner jet and the diffuse component farther from the nucleus implies that the emission mechanisms are similar and supports the hypothesis, suggested in the LF analysis above, that the the unresolved

TABLE 4
BEST-FIT PARAMETERS FOR FOUR CEN A JET REGIONS

Feature	Box (arcmin)	Rate ($\times 10^{-2}$ counts s^{-1})	Photon Index	N_H (PL; $\times 10^{21}$)	Luminosity ($\times 10^{39}$ ergs s^{-1})
Knots AX1 and AX2.....	0.18 \times 0.11	3.7 \pm 0.2	2.5 \pm 0.05	7.2 \pm 0.3	3.31
Knots AX3–AX6.....	0.48 \times 0.22	2.6 \pm 0.3	2.2 \pm 0.1	6.7 \pm 0.8	1.45
Knot B.....	0.38 \times 0.27	5.3 \pm 0.3	2.0 \pm 0.05	2.0 \pm 0.3	1.47
Beyond knot B.....	1.93 \times 0.43	4.1 \pm 0.2	2.3 \pm 0.1	1.7 \pm 0.5	1.27

NOTE.—Summary of the best-fit (0.4–5 keV) parameters for four regions of Cen A jet using an absorbed power-law model. The first column identifies the feature, the second is the size of the region around the feature used for spectral analysis, the third is the background-subtracted count rate from the feature and the statistical (1σ) uncertainty, the fourth is the best-fit photon index and uncertainty, the fifth is the best-fit absorbing column (cm^{-2}), and the sixth is the intrinsic (i.e., unabsorbed) luminosity in the 0.1–10 keV bandpass. The Galactic column density in the direction of Cen A is 7×10^{20} cm^{-2} . All uncertainties on best-fit parameters are the 1σ confidence intervals for two interesting parameters.

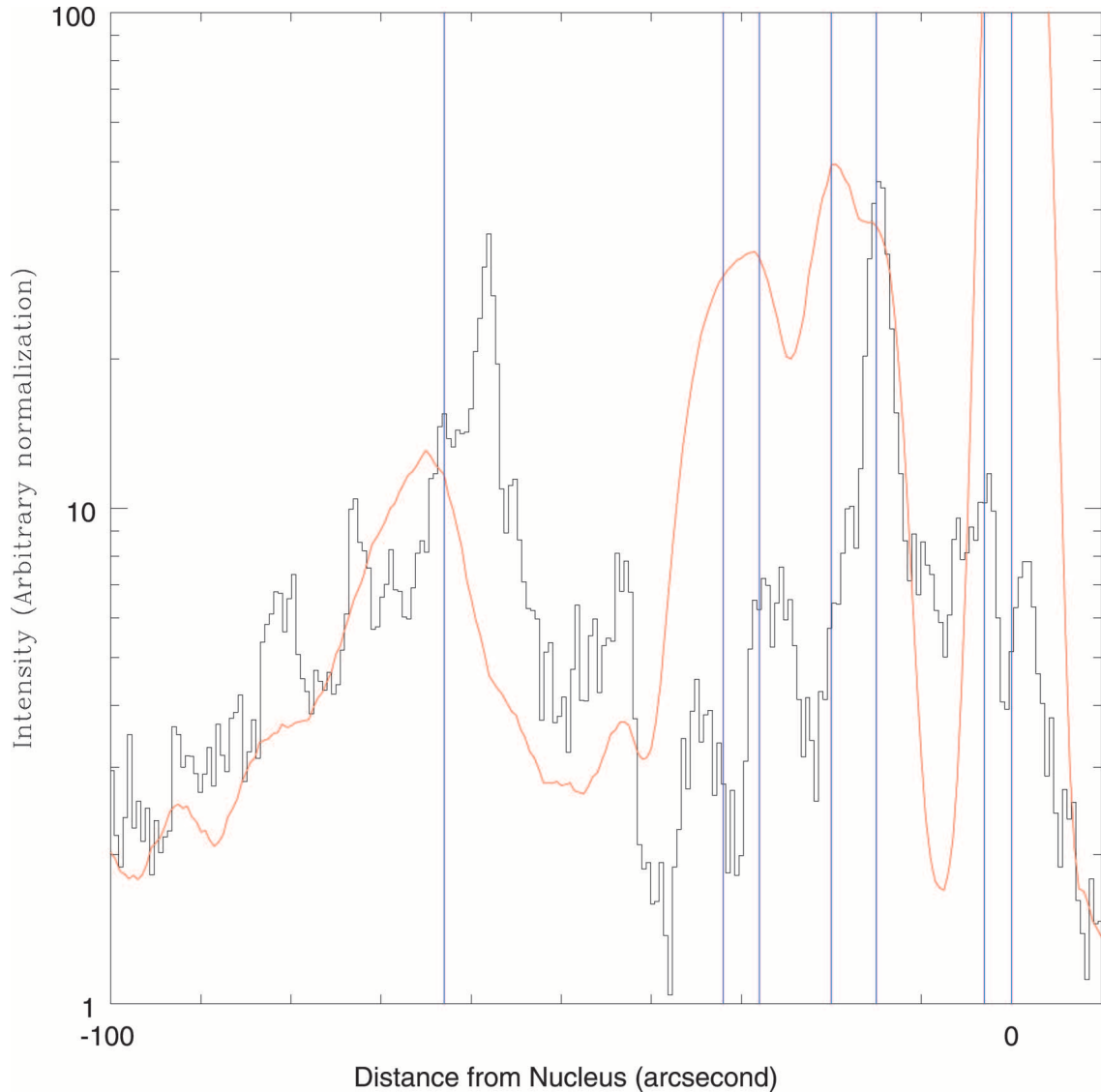


FIG. 12.—Intensity profile (arbitrary normalization) of the X-ray jet in the 0.4–1.8 keV bandpass along position angle 55° in a region $24''$ wide (*black histogram*). The solid curve (*red*) is the radio flux density at 3.6 cm (arbitrary normalization) along the same projection. The positions of the nucleus and the radio knots N1, A1, A2, A3, A4, and B from previous radio observations (Burns et al. 1983) are shown as the blue vertical lines. The slight difference in position of the peak of knot A1 is consistent with the uncertainties in the absolute alignment. The differences in position between the peaks of X-ray and radio emission of the other knots are clearly visible.

diffuse emission is composed of many lower luminosity, spatially unresolved knots.

3.4. Radio to X-Ray Spectral Index

We have determined the radio to X-ray spectral index for each of the bright radio and X-ray knots in the inner jet. Even though the X-ray and radio peaks are misaligned, there is detectable X-ray emission between the radio knots and vice versa. We measured the X-ray count rate and radio flux density at 8.4 GHz in $4''$ wide boxes centered on each of seven X-ray and three radio peaks of the inner jet and in the vicinity of radio knot B. The X-ray count rates were converted to flux densities at 1 keV assuming a photon index of 2.2. For the X-ray knots (excluding knot AX1), we find that the spectral indices between the X-ray and radio bands vary between 0.80 and 0.97 (average 0.90), and the radio knots (again excluding AX1) vary between 0.99 and 1.01. The flux densities and spectral indices are summarized in Table 5. Even though there are significant (factor of 3) variations in

the ratio of X-ray to radio flux along the jet (Fig. 12), the differences in the spectral index between the X-ray peaks and radio peaks are only ~ 0.1 – 0.15 . All of these indices are considerably steeper than the radio spectral indices (20 cm to 6 cm) previously reported (Feigelson et al. 1981), implying spectral steepening between the radio and the X-ray. We note that these radio to X-ray indices are remarkably similar to those measured for the jet in the FR I galaxy 3C 66B (Hardcastle et al. 2001) but considerably steeper than that of 3C 273 (Marshall et al. 2001; Sambruna et al. 2001).

4. DISCUSSION

To summarize, we find that the X-ray morphology of the jet consists of an unresolved, “diffuse” component that extends from within at least ~ 50 pc ($\sim 3''$) of the nucleus to ~ 4 kpc and contains at least 31 distinct spatially resolved X-ray enhancements embedded within diffuse emission. The width of the diffuse component of the inner jet is roughly

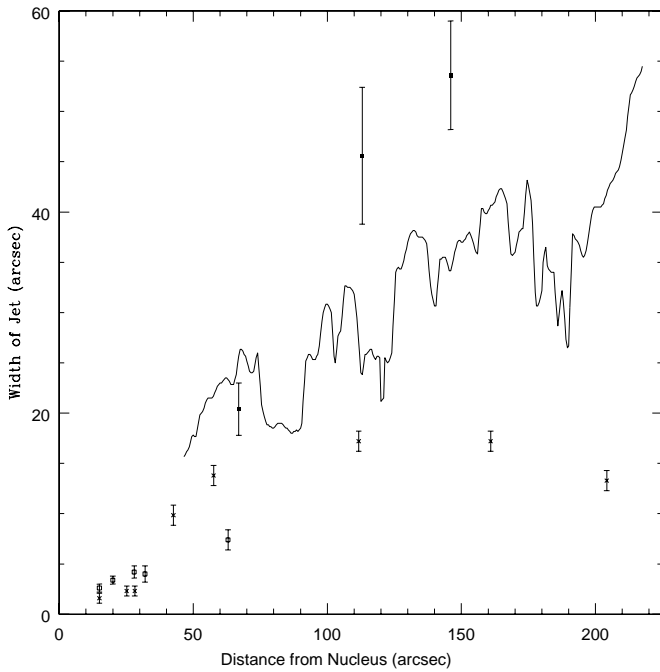


FIG. 13.—Transverse width of jet as a function of distance from the nucleus. The crosses are the width of the X-ray jet (see eq. [1]) measured from our *Chandra* observations, and the open and filled squares are the widths of the jet at 20 cm at high and low resolutions, respectively, taken from Table 2 of Burns et al. (1983). The solid curve is the width of the jet at 3.6 cm measured from the data shown in Fig. 10.

constant to knot AX6, where it widens, although there appears to be a bend or twist in the jet between knots AX2 and AX3 in this inner jet region. In the vicinity of knot B, the jet widens again. Beyond knot F, the jet appears to narrow, but this may be the result of a decrease in the surface

TABLE 5
RADIO TO X-RAY SPECTRAL INDICES

Knot	Radio (mJy)	X-Ray (mJy)	α_{rx}
X-Ray Peak Centered			
NX1.....	23	5.8	0.88
AX1.....	333	110	0.86
AX2.....	247	14	0.97
AX3.....	450	28	0.97
AX4.....	199	14	0.96
AX6.....	46	23	0.84
BX2.....	58	66	0.80
BX5.....	497	50	0.94
Radio Peak Centered			
A1r.....	324	106	0.87
A2r.....	519	22	0.99
A3/4r.....	503	15	1.01

NOTE.—Summary of radio to X-ray spectral indices for knots of the inner jet region. The first column is the knot label, the second is the radio (8.4 GHz) flux density, the third is the X-ray (1 keV) flux density, and the fourth is the radio to X-ray energy spectral index. Each of these flux densities and spectral indices was computed from a box region $4''$ on a side.

brightness of the diffuse component. There are significant differences between the X-ray and radio morphologies in the inner jet region. The spectra of the knots and diffuse emission of the jet are well fitted by both absorbed power-law and absorbed thermal models, but there is no direct evidence for any emission lines in the spectra. What do these results tell us about the nature of the X-ray emission?

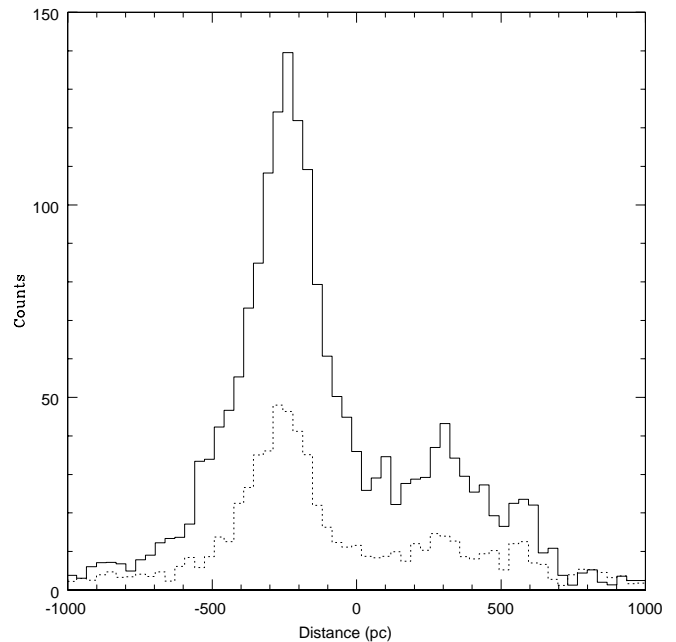
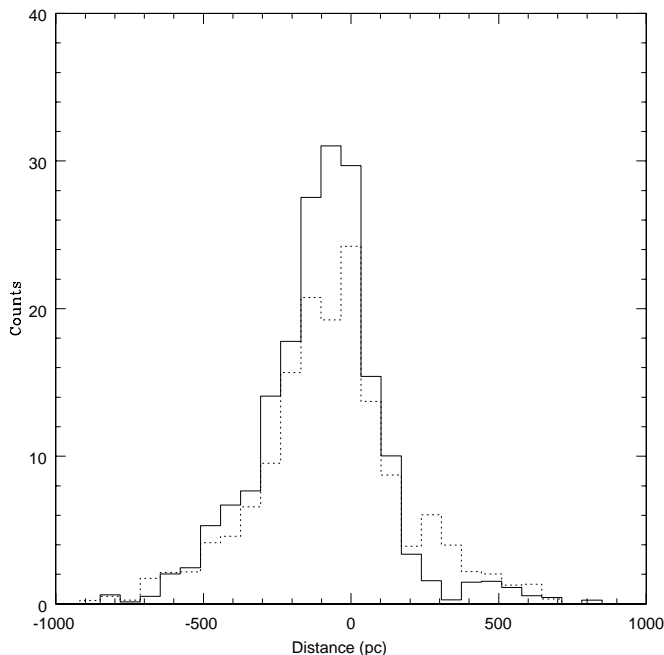


FIG. 14.—Projection of the jet along position angle 55° showing the transverse width in two energy bands: 0.4–1.5 keV (solid line) and 1.5–5.0 keV (dashed line). The data from the two observations have been co-added. The left-hand figure is the projection of the region between knots AX1 and AX4, inclusive, and the right-hand figure is the knot B region. See Table 3 for definition of the regions. For a given region, the width of the jet in the two energy bands is the same. The difference in relative normalization in the two energy bands between the two regions shown here is the result of the larger N_H of the first region.

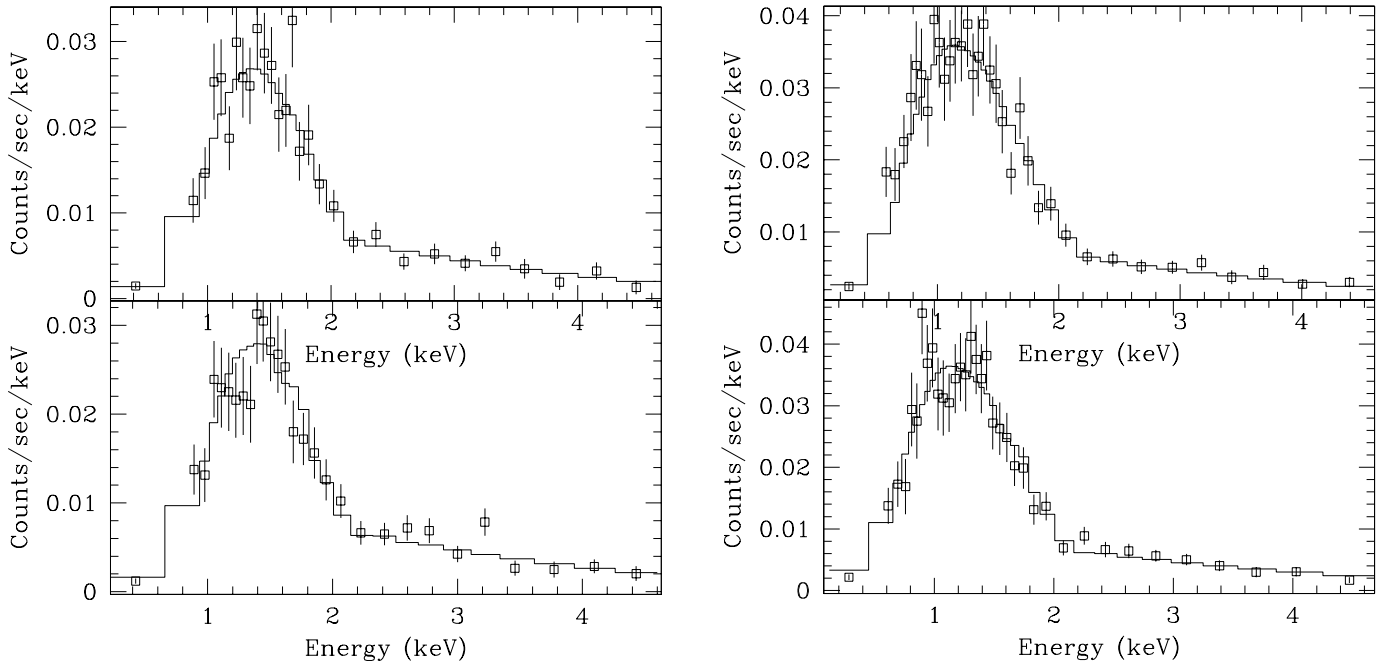


FIG. 15.—Spectra and best-fit absorbed power-law model of knot AX1/2 (*left*) and knot B (*right*). The spectra on the top are the data from the first observation (OBSID 00316), and those on the bottom are from the second (OBSID 00962). The best-fit parameters are summarized in Table 4.

Generally, four models are typically invoked to explain X-ray emission from extragalactic jets and the hotspots in radio lobes: thermal emission, synchrotron self-Compton (SSC) emission, inverse Compton scattering from an external source of seed photons, and synchrotron emission from a population of ultrarelativistic electrons (Harris 2002). The first three have been rejected by previous authors (Feigelson et al. 1981; Burns et al. 1983) for the Cen A jet, and this work does not alter those conclusions. The thermal model was ruled out because of the relatively high density of thermal plasma required to explain the emission. This plasma would be overpressured relative to the surrounding medium, and it would therefore be difficult to confine this plasma within a small volume. The knots would rapidly dissipate. In addition, Faraday rotation and depolarization measurements put upper limits on the density of material in such thermal knots that are well below that required to account for the observed emission. The absence of any significant spectral features observed in our data strengthens this conclusion. We note that recent *Chandra* High Energy Transmission Grating Spectrometer observations of the jet of M87 also failed to detect line emission (Miller et al. 2000). Inverse Compton scattering of the cosmic microwave background has been successful in explaining the X-ray emission from more powerful jets such as 3C 273 (Sambruna et al. 2001) and PKS 0637–752 (Celotti, Ghisellini, & Chiaberge 2001), but only by invoking a large bulk Lorentz factor for a jet placed at small angle to the line of sight. It is believed, however, that the Cen A jet lies at a large angle (50° – 80°) to our line of sight (Jones et al. 1996; Israel 1998; Tingay et al. 1998). The SSC mechanism can be rejected since the density of radio photons is even lower than CMB photons, making any such model even more unlikely. Another possible source of seed photons is beamed optical emission from the active nucleus (Pérez-Fournon 1985). In the unified model of active galactic nuclei, Cen A is considered to be a misdirected BL Lac object (Urry & Padovani 1995), so the

beamed emission from the nucleus, unseen by us, could be quite large (Fossati et al. 1998). Electron energies of $\gamma \sim 25$ are required to boost optical photons into the X-ray regime. At knot A1, the synchrotron frequency of these low-energy electrons is below 1 MHz (assuming the equipartition magnetic field of $61 \mu\text{G}$), which is unobservable. The observed X-ray spectral index (energy index 0.9–1.4) of the inner jet, however, is much steeper than the radio spectral index (0.4–0.6) between 1.4 and 4.87 GHz. Unless the spectral index of the unseen electrons is dramatically steeper than that of the electrons producing the observed radio emission, it is not possible for a significant fraction of the X-ray emission to result from this mechanism because of these spectral differences.

On the basis of the morphological similarities between the radio and X-ray emission and the limitations of competing models, it has been concluded previously that both the X-ray and radio flux from the jet originate in synchrotron emission from a population of ultrarelativistic electrons. The knots are presumably sites of shocks where particles are accelerated to $\gamma \sim 10^7$ – 10^8 to produce the observed X-ray emission, assuming an equipartition magnetic field (Feigelson et al. 1981; Burns et al. 1983). The main argument against a synchrotron hypothesis has been that the lifetime due to synchrotron emission of the ultrarelativistic particles is considerably less than the travel time down the jet, thus requiring that the particles be reaccelerated (Feigelson et al. 1981), perhaps multiple times, as they travel along the jet to the radio lobe. In fact, in the inner jet region, the particles must undergo local accelerations multiple times within a knot. The lifetime of the X-ray emitting electrons in the inner jet is ~ 20 yr, an order of magnitude less than the travel time from the nucleus to knot B. The lifetime of the particles beyond knot B is longer (~ 60 yr) because of the lower magnetic field but is still considerably less than the travel time into the radio lobe. Based on estimates of the knot sizes from *Einstein* observations (hundreds of parsecs), it was

argued that the large volumes of the knots pushed acceleration models to their limits (Burns et al. 1983). This criticism is considerably weakened based on our *Chandra* observations because each previously observed X-ray knot is actually composed of several smaller knots. Thus, the knot volume and the shock sizes are considerably smaller (tens of parsecs rather than hundreds of parsecs) than previously supposed. Local acceleration of the electrons within the knots, however, is still a necessary component of this model.

The morphological differences between the X-ray and radio emission complicate this simple model for the emission. These differences argue strongly against the simple hypothesis that a single spatially coincident population of relativistic electrons is responsible for both the X-ray and radio emission (Feigelson et al. 1981; Burns et al. 1983) in the nuclear and inner jet regions, except perhaps at knots N1/NX1 and A1/AX1. Our data support a model in which the X-ray emission is indeed synchrotron radiation from relativistic particles, but the radio emission originates, at least in part, from a spatially distinct, less energetic population of electrons.

The only other extragalactic jet that has been as well studied as the Cen A jet is that in M87, and there are some remarkable morphological similarities between the two jets. Small differences between the X-ray, optical, and radio morphology of the jet in M87 on roughly the same spatial scale as those described here have been reported (Neumann et al. 1997; Sparks, Biretta, & Macchetto 1996; Perlman et al. 1999). In particular, recent *Chandra* observations of the M87 jet have detected morphological differences remarkably similar to those seen here (Perlman, Marshall, & Biretta 2002; Marshall et al. 2002). *HST* imaging and polarimetric observations of M87 have provided evidence that the more energetic particles responsible for the optical and X-ray emission from the M87 jet are located closer to the axis of the jet, which is surrounded by a sheath or cocoon of lower energy particles responsible for the radio emission. The knots in the M87 jet are identified as the sites of shocks in the flow where the magnetic fields are compressed and the particles accelerated (Sparks et al. 1996; Perlman et al. 1999). The optical and X-ray emission is then the result of synchrotron radiation at the sites of the shocks. Differences between the optical and radio emission are caused by particle diffusion and aging. A similar model can be used to qualitatively describe all the features of the bright X-ray/radio knots of the Cen A inner jet. The differences in the positions of the knots in the X-ray and radio emission are naturally explained by particle aging. This hypothesis could be greatly strengthened if optical emission could be detected between the various radio and X-ray knots, but the dark dust lane makes such a detection unlikely (Marconi et al. 2000). In fact, it is now becoming clear that such morphological differences are a common feature of X-ray and radio emission from FR I galaxies (Hardcastle et al. 2001). The existence of shock sites and the generation of X-ray-emitting plasma may be a fundamental feature of jets in FR I galaxies.

5. SUMMARY AND CONCLUSIONS

We have presented high-resolution *Chandra*/ACIS-I X-ray images and spectra of the X-ray jet in Centaurus A and have found the following:

1. In the inner arcminute of the jet, there are significant morphological differences between the radio and X-ray emission. The X-ray and radio positions of the two knots closest to the nucleus (NX1 and AX1) agree to within the precision of our absolute astrometry ($0''.5$), but beyond knot AX1 (~ 250 pc from the nucleus) there are significant differences up to ~ 90 pc between the positions of the X-ray and radio peaks.

2. Given the offsets of the radio and X-ray knots, there are large (factor of ~ 3) variations in the ratio of X-ray to radio flux in the inner jet region. In the inner jet and the vicinity of radio knot B, the radio to X-ray spectral indices of the X-ray bright knots and radio bright knots are about 0.9 and 1.0, respectively.

3. At a linear resolution of ~ 30 pc ($1''.5$) the jet contains at least 31 knots or enhancements in X-ray emission embedded within continuous diffuse emission extending about 4 kpc from the nucleus. Each previously observed X-ray knot is composed of several knots embedded within diffuse emission.

4. The spectra of several regions of the jet are well fitted by an absorbed power-law model, and although we cannot exclude thermal models, there is no statistically significant evidence for any emission lines. The spectrum of the jet beyond knot B, which is dominated by the diffuse, unresolved component, is similar to that of the bright knots of the inner jet.

5. At the bright X-ray knot AX1, the width of the jet in the X-ray and radio bandpasses is similar. Beyond this knot into the northeast radio lobe, however, the X-ray jet appears to be narrower than the radio jet. The X-ray jet appears to be well collimated from the nucleus into the northeast radio lobe.

These results strengthen the case that the X-ray emission from the Cen A jet results from synchrotron radiation from ultrarelativistic particles and that the knots are shock sites where the particles are reenergized as they travel along the jet. There are strong arguments against thermal and inverse Compton models for the X-ray emission, none of which has been negated by these observations. The strongest arguments against the synchrotron hypothesis were the large shock volume, the difficulty of particle reenergization, and the necessity of multiple reacceleration within a knot. These have been significantly weakened by this observation since the sizes of the knots are considerably smaller (tens of parsecs rather than hundreds) than previously supposed. In addition, both the spectra and the radio/X-ray morphological differences we observe are consistent with the synchrotron hypothesis.

Chandra has now detected X-ray emission from the jets of a significant number of FR I radio galaxies (Worrall et al. 2001; Harris 2002). The radio/X-ray morphologies, the spectral indices, and the X-ray spectra of these objects are remarkably similar to those of Cen A. We suggest that X-ray emission may, in fact, be a common aspect of the jets in these galaxies, and that the shock acceleration of particles to $\gamma \sim 10^7$ – 10^8 may be an integral feature of the hydrodynamics of such jets. *Chandra* will allow us to make a systematic study of the X-ray emission from extragalactic jets to better assess the relationship between bulk flows and particle acceleration.

This work was supported by NASA contracts NAS 8-38248 and NAS 8-39073, the Chandra Science Center, and the Smithsonian Institution. We are grateful to Jack Burns for allowing us to use his archival VLA observations of

Cen A. We would also like to thank Herman Marshall for discussing the results of the *Chandra* observations of the M87 jet before publication.

REFERENCES

- Aldcroft, T. A., Karovska, M., Cresitello-Dittmar, M. L., Cameron, R. A., & Markevitch, M. L. 2000, *Proc. SPIE*, 4012, 650
- Biretta, J. A., Stern, C. P., & Harris, D. E. 1991, *AJ*, 101, 1632
- Brodie, J., & Bowyer, S. 1985, *ApJ*, 292, 447
- Burns, J. O., Feigelson, E. D., & Schreier, E. J. 1983, *ApJ*, 273, 128 (BFS83)
- Celotti, A., Ghisellini, G., & Chiaberge, M. 2001, *MNRAS*, 321, L1
- Chandra* Proposers' Observatory Guide, Rev. 3.0, 2001
- Chartas, G., et al. 2000, *ApJ*, 542, 655
- Clarke, D. A., Burns, J. O., & Norman, M. L. 1992, *ApJ*, 395, 444
- Döbereiner, S., et al. 1996, *ApJ*, 470, L15
- Feigelson, E. D., Schreier, E. J., Delvaile, J. P., Giacconi, R., Grindlay, J. E., & Lightman, A. P. 1981, *ApJ*, 251, 31 (F81)
- Fossati, G., Maraschi, L., Celotti, A., Comastri, A., & Ghisellini, G. 1998, *MNRAS*, 299, 433
- Hardcastle, M. J., Birkinshaw, M., & Worrall, D. M. 2001, *MNRAS*, 326, 1499
- Harris, D. E. 2002, in *ASP Conf. Ser. 250, Particles and Fields in Radio Galaxies*, ed. Robert A. Laing & Katherine M. Blundell (San Francisco: ASP), in press
- Israel, F. P. 1998, *A&A Rev.*, 8, 237
- Jones, D. L., et al. 1996, *ApJ*, 466, L63
- Joy, M., Harvey, P. M., Tollestrup, E. V., Sellgren, K., McGregor, P. J., & Hyland, A. R. 1991, *ApJ*, 366, 82
- Kraft, R. P., et al. 2000, *ApJ*, 531, L9
- Kraft, R. P., Kregenow, J. M., Forman, W. R., Jones, C., & Murray, S. S. 2001, *ApJ*, 560, 675
- Marconi, A., Schreier, E. J., Koekemoer, A., Capetti, A., Axon, D., Macchetto, D., & Caon, N. 2000, *ApJ*, 528, 276
- Marshall, H. L., et al. 2001, *ApJ*, 549, L167
- Marshall, H. L., Miller, B. P., Davis, D. S., Perlman, E. S., Canizares, C. R., Harris, D. E., & Biretta, J. A. 2002, *ApJ*, 564, 683
- Miller, B. P., Marshall, H. L., Davis, D. S., Wise, M. W., Matsumoto, H., & Canizares, C. 2000, *BAAS*, 197, 12503
- Monet, D. 1998, *BAAS*, 193, 12003
- Morganti, R., Fosbury, R. A. E., Hook, R. N., Robinson, A., & Tsvetanov, Z. 1992, *MNRAS*, 256, 1P
- Morganti, R., Robinson, A., Fosbury, R. A. E., di Serego Alighieri, S., Tadhunter, C. N., & Malin, D. F. 1991, *MNRAS*, 249, 91
- Neumann, M., Meisenheimer, K., Röser, H.-J., & Fink, H. H. 1997, *A&A*, 318, 383
- Pérez-Fournon, I. 1985, in *Active Galactic Nuclei*, ed. J. E. Dyson (Manchester: Manchester Univ. Press), 300
- Perlman, E. S., Biretta, J. A., Zhou, F., Sparks, W. B., & Macchetto, F. D. 1999, *AJ*, 117, 2185
- Perlman, E. S., Marshall, H. L., & Biretta, J. A. 2002, in *ASP Conf. Ser. 255, Mass Outflow in Active Galactic Nuclei: New Perspectives*, ed. D. M. Crenshaw, S. B. Kraemer, & I. M. George (San Francisco: ASP), in press
- Sambruna, R. M., Urry, M. C., Tavecchio, F., Maraschi, L., Scarpa, R., Chartas, G., & Muxlow, T. 2001, *ApJ*, 549, L161
- Schiminovich, D., van Gorkom, J. H., van der Hulst, J. M., & Kasow, S. 1994, *ApJ*, 423, L101
- Schreier, E. J., Capetti, A., Macchetto, F., Sparks, W. B., Ford, H. J. 1996, *ApJ*, 459, 535
- Schreier, E. J., Feigelson, E., Delvaile, J., Giacconi, R., Grindlay, J., Schwartz, D. A., & Fabian, A. C. 1979, *ApJ*, 234, L39
- Smith, R. K., & Dwek, E. 1998, *ApJ*, 503, 831
- Sparks, W. B., Biretta, J. A., & Macchetto, F. 1996, *ApJ*, 473, 254
- Stark, A. A., Gammie, C. F., Wilson, R. W., Bally, J., Linke, R. A., Heiles, C., & Hurwitz, M. 1992, *ApJS*, 79, 77
- Tingay, S. J., et al. 1998, *AJ*, 115, 960
- Turner, T. J., George, I. M., Mushotzky, R. F., & Nandra, K. 1997, *ApJ*, 475, 118
- Urry, C. M., & Padovani P. 1995, *PASP*, 107, 803
- Vikhlinin, A., Forman, W., Jones, C., & Murray, S. 1995, *ApJ*, 451, 542
- Weisskopf, M. C., Tananbaum, H. D., Van Speybroeck, L. P., & O'Dell, S. L. 2000, *Proc. SPIE*, 4012, 2
- Wise, M. W., Huenemoerder, D. P., & Davis, J. E. 1997, in *ASP Conf. Ser. 125, Astronomical Data Analysis Software and Systems VI*, ed. G. Hunt & H. E. Payne (San Francisco: ASP), 447
- Worrall, D. M., Birkinshaw, M., & Hardcastle, M. J. 2001, *MNRAS*, 326, 7